Elucidating the dechlorination mechanism of hexachloroethane by Pd-doped zerovalent iron microparticles in dissolved lactic acid polymers using chromatography and indirect monitoring of iron corrosion

Romain Rodrigues, Stéphanie Betelu, Stefan Colombano, Guillaume Masselot, Théodore Tzedakis, Ioannis Ignatiadis

Elucidating the dechlorination mechanism of hexachloroethane by Pd-doped zero-valent iron microparticles in dissolved lactic acid polymers using chromatography and indirect monitoring of iron corrosion

Romain Rodrigues[1,2,3*], Stéphanie Betelu[1], Stéfan Colombano[1], Guillaume Masselot[2], Theodore Tzedakis[3], Ioannis Ignatiadis[1]

1: BRGM (French Geological Survey), 3 avenue Claude Guillemin, 45060 Orléans Cedex 2, France.

2: ADEME (French Environment and Energy Management Agency), 20 avenue du Grésillé, 49000 Angers Cedex 1, France.

3: LGC (Chemical Engineering Laboratory), 118 route de Narbonne, 31062 Toulouse Cedex 9, France.

* Corresponding author: romain.rodrigues64@gmail.com

Abstract

The degradation mechanism of the pollutant hexachloroethane (HCA) by a suspension of Pd-doped zero-valent iron microparticles (Pd-mZVI) in dissolved lactic acid polymers and oligomers (referred to as PLA), was investigated using gas chromatography and the indirect monitoring of iron corrosion by continuous measurements of pH, oxidation-reduction potential (ORP) and conductivity. The first experiments took place in the absence of HCA, to understand the evolution of the Pd-mZVI/PLA/H_2O system. This showed that the evolution of pH, ORP and conductivity is related to changes in solution chemistry due to iron corrosion, and that the system is initially cathodically controlled by H^+ mass transport to Pd surfaces because of the presence of an extensive PLA layer. We then investigated the effects of Pd-mZVI particles, temperature, initial HCA concentration and PLA content on the Pd-mZVI/PLA/HCA/H_2O system, to obtain a better understanding of the degradation mechanism. In all cases, HCA dechlorination first requires the production of atomic hydrogen H^*—involving the accumulation of tetrachloroethylene (PCE) as an intermediate—before its subsequent reduction to non-chlorinated C_2 and C_4 compounds. The ratio between Pd-mZVI dosage, initial HCA concentration and PLA content affects the rate of H^* generation as well as the rate-determining step of the process. A pseudo-first-order equation can be applied when Pd-mZVI dosage is much higher than the theoretical stoichiometry (600 mg for $[HCA]_0$ = 5-20 mg L^{-1}). Our results indicate that the HCA degradation mechanism includes mass transfer, sorption, surface reaction with H^*, and desorption of the product.

Keywords

Hexachloroethane; Pd/Fe microparticles; Iron corrosion; Physical and chemical monitoring; Dechlorination mechanism; Lactic acid polymers

1. Introduction

Since the first application of zero-valent iron (ZVI) as granular particles in permeable reactive barriers (PRBs) for *in situ* remediation of contaminated groundwater in the 1990s (Gillham and O'Hannesin 1994; O'Hannesin and Gillham 1998), ZVI has been the subject of widespread research to improve the reactivity, stability and transport of such particles in the subsurface environment (Zhang 2003; Crane and Scott 2012; O 'Carroll et al. 2013; Yan et al. 2013; Tosco et al. 2014; Liu et al. 2014b; Fu et al. 2014; Zhao et al. 2016; Reddy et al. 2016; Stefaniuk et al. 2016; Sun et al. 2016; Mu et al. 2017). The use of microscale ZVI (mZVI) particles appears to be a sustainable option, as they are less expensive and less bactericidal, and have a longer life in field experiments

than nanoscale ZVI (nZVI) particles (Lee et al. 2008; Comba et al. 2011; Noubactep et al. 2012; Velimirovic et al. 2012, 2013a, 2018). However, irrespective of their size, iron particles have a low electron efficiency toward contaminants and react mainly with water to produce Fe^{2+} and H_2 (Schöftner et al. 2015; Fan et al. 2016; Tang et al. 2017b). It was realized that bimetallic particles, especially Pd-ZVI ones, can be used to increase the degradation rate by taking advantage of the hydrogenation reactions that generate atomic hydrogen H^* on the second metal (Lowry and Reinhard 1999; Kim and Carraway 2003; Lien and Zhang 2007; Xie and Cwiertny 2013; Liu et al. 2014b). Finally, the use of a polymeric coating is essential for improving the stability, dispersion and transport of the particles in groundwater (He et al. 2007; Phenrat et al. 2008; Kaifas et al. 2014; Kocur et al. 2014; Reddy et al. 2014; Han et al. 2016; Kumar et al. 2017; Fang et al. 2018).

Despite these improvements, the exact mechanism of contaminant removal by iron-based particles still remains unclear. The particles have a core-shell structure, with an Fe^0-core encapsulated by a thin, defective and semiconducting shell of mixed-valence Fe_xO_y iron oxides (Martin et al. 2008; Filip et al. 2014; Liu and Zhang 2014; Ling et al. 2017; Bae et al. 2018). This shell is known to be the seat of all contaminant remediation processes through a combination of adsorption, reduction and co-precipitation processes (Noubactep 2008). For bimetallic particles, the presence of the second metal results in the formation of galvanic cells, Fe acting as an anode and preferentially oxidized and the second metal acting as the main cathodic site (Grittini et al. 1995; Lien and Zhang 1999), which implies that the reduction process occurs mainly on its surface. In both cases, the growth and structural evolution of the shell with time in the ZVI/H_2O system—also known as aging—generally results in a decrease of its porosity and electrical conductivity (Mu et al. 2017) and in the entrapment of the second metal (Yan et al. 2010; Ling and Zhang 2014), affecting the kinetics of iron oxidation and thus all degradation processes (Kumar et al. 2014; Liu et al. 2017). Understanding the evolution of ZVI particles and its impact on the solution chemistry is therefore crucial for evaluating their reactivity, fate and other effects.

Direct characterization methods, such as microscopic and spectroscopic techniques or total-iron measurements (Nurmi et al. 2005; Sun et al. 2006; Sarathy et al. 2008; Baer et al. 2008), require the recovery of solids and sample stabilization, which can be hardly feasible in the field. Such techniques are useful for characterizing the structural evolution of the iron-oxide shell, but they do not provide direct quantitative evidence of iron corrosion. Corrosion rates are commonly estimated by indirect characterization methods, especially hydrogen production measurements (Liu and Lowry 2006; Velimirovic et al. 2014), but this method is unsuitable for Pd-ZVI particles as hydrogen sorption occurs on the Pd surface (Chaplin et al. 2012). Other indirect methods focus on changes in the solution chemistry, e.g. pH and oxidation-reduction potential (ORP), due to the addition of ZVI particles and

69 the resulting reactions in the ZVI/H_2O system (Yu et al. 2014). In field applications, though the complex water
70 chemistry can alter the individual characterization ability of these methods, such indirect methods can show up
71 evidence for ZVI-impacted zones due to the transport of iron-corrosion products, with their associated changes
72 in biogeochemical conditions (Elliott and Zhang 2001; He et al. 2010; Wei et al. 2010, 2012, Shi et al. 2011,
73 2015; Kocur et al. 2014). The combined use of probes appears therefore as an effective tool for understanding
74 both the reactivity and fate of iron-based particles over short- and long-term time scales (Grieger et al. 2010; Shi
75 et al. 2015).

76 In our previous study, we showed that the use of continuous pH and ORP measurements was effective in
77 laboratory experiments for characterizing the degradation mechanism of hexachlorobutadiene (HCBD) by Pd-
78 doped ZVI microparticles (noted Pd-mZVI) suspended in dissolved lactic acid polymers and oligomers (referred
79 to as PLA) (Rodrigues et al. 2017a). PLA is a low-cost biodegradable polymer, widely used for the
80 denitrification of water (Wang and Chu 2016), which we selected as surface modifier to (i) Increase the viscosity
81 of the suspension for preventing aggregation, (ii) Provide hydrophobicity on the particle surface for improving
82 the contact with the hydrophobic pollutant, and (iii) Create acidic conditions through PLA hydrolysis and the
83 release of organic acids for obtaining optimal conditions for the reductive dechlorination of highly chlorinated
84 organic compounds. In addition, in field experiments, PLA acts as a slow-release source of carbon and hydrogen
85 that can stimulate biodegradation by organohalide-respiring bacteria, to maintain reductive conditions over the
86 long term. The efficiency of polyesters, such as polyhydroxyalkanoates (PHA), has already been proven for the
87 bioremediation of COCs (Aulenta et al. 2008; Pierro et al. 2017). The use of ZVI-based particles with a
88 biodegradable slow-release carbon and hydrogen source appears thus as a sustainable strategy for creating an *in*
89 *situ* reactive zone for pollution treatment. It combines the reactivity of a short-term chemical treatment—
90 especially for highly chlorinated and recalcitrant contaminants—with maintaining reductive conditions for long-
91 term bioremediation, in order to prevent a potential rebound effect after the aging of iron-based particles (Baric
92 et al. 2012; Bruton et al. 2015; Koenig et al. 2016; Kocur et al. 2016; Chronopoulou et al. 2016; Xu et al. 2017;
93 Herrero et al. 2019).

94 The objective of our study was to elucidate the degradation mechanism of hexachloroethane (HCA, C_2Cl_6) using
95 Pd-mZVI in PLA, through the indirect monitoring of iron corrosion and its associated changes in solution
96 chemistry by means of continuous measurements of pH, ORP and conductivity. HCA is a common highly
97 chlorinated pollutant found in soil and groundwater, with a low aqueous solubility (Rodrigues et al. 2017b). It is
98 mainly used in the production of pyrotechnic devices and metal alloys, but it can also be a by-product of

fabricating lower chlorination products (Stringer and Johnston 2001). Though HCA is known to be relatively persistent in the environment (Howard 1989), it can undergo reductive dechlorination (Butler and Hayes 1998; Patterson et al. 2001; Lien and Zhang 2005; Song and Carraway 2005; Wu et al. 2014; Zhu et al. 2018). Many chlorinated intermediates can accumulate during this transformation, especially chlorinated ethanes, ethylenes and acetylenes, some of them (TCE and vinyl chloride) being classified as human carcinogens by IARC.

Understanding the HCA degradation mechanism is therefore important for preventing any accumulation of toxic byproducts. Experiments were first done in the absence of HCA for evaluating any changes in the Pd-mZVI/PLA/H_2O system. We then investigated the effects of Pd-mZVI particles, temperature, initial HCA concentration and PLA content on the Pd-mZVI/PLA/HCA/H_2O system, to provide a better insight into the degradation mechanism.

2. Materials and methods

2.1. Chemicals

HCA (99%) and tetrachloroethylene (PCE, 99%) were purchased from Sigma-Aldrich. A mix of chlorinated hydrocarbons in methanol (200 µg mL^{-1}) containing chlorinated ethanes and ethylenes was obtained from Sigma-Aldrich for the preparation of standard solutions (EPA 502/524.2 VOC Mix). Stock solutions of HCA (5, 10 and 20 g L^{-1}) were prepared in HPLC-grade methanol, supplied by VWR. Deionized water was obtained from a Milli-Q water system (18.2 MΩ cm) and was degassed before any experiment with an ultrasonic bath at 45 kHz, followed by N_2 flushing during the preparation of batch experiments to limit the introduction of O_2.

The—partially biologically produced—Pd-doped iron microparticles (BioCAT, noted as Pd-mZVI) and the mixture of lactic acid polymers and oligomers dissolved in ethyl lactate (Dechlorem, noted as PLA) were provided by Biorem Engineering. According to the manufacturer, the particles are smaller than 10 µm with an average size of 3-5 µm, palladium representing 0.1-2 wt% of the particles. The specific surface area, measured with the BET-N_2 adsorption method (BELSORP-max, MicrotracBEL, Japan), was less than 1 m^2 g^{-1}. The suspension of Pd-mZVI in PLA was prepared before any experiments by manual mixing of the corresponding amounts of PLA and Pd-mZVI.

For the system without HCA, the experiments were also performed with nZVI particles (NANOFER STAR, obtained from Nano Iron), and the results are presented in the Supplementary data.

126 *2.2. Batch experiments*

127 Batch experiments were conducted in a 1 L cylindrical Pyrex double-walled water-jacketed reactor, equipped
128 with a mechanical-propeller stirring rod (at 300 rpm). The reactor head has hermetic ports for installing the
129 electrodes, for the introduction of the reactant and for sampling. 1 mL of the appropriate stock solution was
130 injected into the reactor filled with degassed deionized water with initial zero-headspace conditions. Reaction
131 was initiated by introducing the Pd-mZVI suspension in PLA, and 3 mL aliquots were collected at selected
132 times. The reduction was stopped by separating the particles with powerful magnets. 1 mL of the supernatant
133 aqueous phase without particles was collected and diluted (1:10) with degassed pure water into 20 mL headspace
134 vials equipped with a PTFE septum. The prepared samples were finally stocked at 4 °C and analysed within 24
135 hours.

136 *2.3. Analytical methods*

137 The bimetallic microparticles were characterized before any reaction by scanning electron microscopy coupled
138 to energy dispersive X-ray spectrometry (SEM/EDS), X-ray diffraction (XRD) and X-ray photoelectron
139 spectroscopy (XPS). SEM/EDS images were obtained with a Phenom XL microscope (Fondis Bioritech)
140 operating at 15 kV. XRD analyses were performed with a D8 Advance diffractometer (Bruker) with a CuKα
141 source (λ = 1.5406 Å) at an accelerating voltage of 40 kV and emission current of 40 mA. Samples were scans
142 from 4 to 90° 2θ at 0.03° 2θ s^{-1}. XPS analyses were performed with a K-Alpha+ spectrometer (ThermoFisher
143 Scientific) equipped with a Al anode generating Al K_α X-ray radiation. Samples were analysed at Fe 2p, Pd 3d,
144 C 1s, O 1s, N 1s and Si 2p regions after survey scans.

145 Analysis of HCA and its degradation products was performed by gas chromatography (GC/FID) using a Varian
146 CP-3800 equipped with a DB-624 column (30 m x 0.32 i.d., with a 1.80 µm film thickness). Helium was chosen
147 as carrier gas at a 1.2 mL min^{-1} flowrate. Samples were heated at 80 °C for 30 min, and 200 µL of the headspace
148 gas was withdrawn by a gas-tight syringe and introduced in the injector chamber at 250 °C (1:25 split ratio). The
149 oven was maintained at 35 °C for 5 min, and then ramped up to 245 °C at 10 °C min^{-1} with a hold for 10 min at
150 this final temperature. The FID temperature was maintained at 300 °C, and He was used as carrier gas at a
151 flowrate of 30 mL min^{-1}. Combustion in the FID was carried out with H_2 (30 mL min^{-1}) and air (300 mL min^{-1}).
152 Seven reference standards of chlorinated hydrocarbons, ranging from 50 to 5000 µg L^{-1}, were periodically
153 prepared and analysed to ensure the proper quantification of the samples. The qualitative production of non-
154 chlorinated hydrocarbons is also provided in Supplementary data.

The Pd-mZVI corrosion was monitored by measuring changes in pH, ORP and conductivity with a multi-parameter tester (Heitolab MPC 350, Heito) and recorded every 12 s using a Keithley 2700 data acquisition system controlled via KickStart software. The pH was measured with a glass electrode (Radiometer Analytical pHC3005-8, Hach), calibrated before each experiment with commercial buffer solutions (pH 7 and 4). The oxidation-reduction potential (ORP) of the solution was measured with a platinum disc electrode (Radiometer Analytical XM150, Hach) with respect to a mercury-mercurous sulphate reference electrode (MMSE, Ametek SI). ORP values were then converted and reported with respect to the standard hydrogen electrode (SHE) by adding 640 mV (saturated K_2SO_4 solution). Conductivity was measured with a 2-pole conductivity cell (Tacussel XE 150) and calibrated before each experiment with a commercial buffer solution (1413 µS cm^{-1} at 25 °C). All electrodes were placed in the aqueous solution at about one third of the reactor.

In a non-buffered system (Bae and Hanna 2015), the evolution of pH is a good indicator of iron corrosion as H^+ is directly implied in the reaction (Eq. 1).

$$Fe^0 + 2\,H^+ \rightarrow Fe^{2+} + H_2 \qquad \text{(Eq. 1)}$$

Eq. (1) is the result of iron oxidation in Fe^{2+} and H^+ reduction in H_2. The hydrogen evolution reaction (HER) occurs both on the oxide shell and on Pd. Because of the difference in the standard redox potential, Pd acts as the preferential cathodic site in the system, and the reduction of H^+ in H_2 occurs in a two-step process (Eqs. 2-3).

$$2\,H^+ + 2\,e^- \xrightarrow{Pd} 2\,H^* \qquad \text{(Eq. 2)}$$

$$2\,H^* \rightarrow H_2 \qquad \text{(Eq. 3-1)}$$

$$H^* + H^+ + e^- \rightarrow H_2 \qquad \text{(Eq. 3-2)}$$

The formation of atomic hydrogen H^* on Pd is of crucial importance as adsorbed H^* (H^*_{ads}) is the only active hydrogen species in catalytic hydrodechlorination reactions (Jiang et al. 2017; He et al. 2018; Liu et al. 2018). The cumulative H^+ consumption, or the total generated H^* yield, can be calculated considering the reduction of H^+ to H^* and the dissociation of H_2O into H^+ before its reduction to H^* (Jiang et al. 2018), as indicated in the Supplementary data (Fig. S3).

Measurements of the oxidation-reduction potential (ORP) provide information on the composition and changes in the physico-chemistry of the solution. In the presence of ZVI particles, ORP values are mainly dependent upon iron-species couples (Shi et al. 2011) and the H^+/H_2 redox couple, because of the affinity of Pt (the sensing

probe) to hydrogen adsorption (Papaderakis et al. 2017). Finally, conductivity is an indicator of the ionic content in solution. The conductivity of the solution can be calculated by the equation below (Eq. 4):

$$\sigma = \sum_i \lambda_i z_i C_i \qquad \text{(Eq. 4)}$$

where σ is the conductivity (S m^{-1}), λ_i the molar ionic conductivity of species i (S m^2 mol^{-1}), z_i the electrical charge of species i and C_i the concentration of species i (mol m^{-3}). Considering iron corrosion and HCA dechlorination, the main ionic species that can influence the conductivity are H^+ (at 25 °C, $\lambda°_{H^+}$ = 349.8 S cm^2 mol^{-1}), OH^- ($\lambda°_{OH^-}$ = 198 S cm^2 mol^{-1}), Fe^{2+} ($\lambda°_{1/2Fe^{2+}}$ = 54 S cm^2 mol^{-1}), Fe^{3+} ($\lambda°_{1/3Fe^{3+}}$ = 68 S cm^2 mol^{-1}), Cl^- ($\lambda°_{Cl^-}$ = 76 S cm^2 mol^{-1}), and the ionic species resulting from the introduction and hydrolysis of PLA. The decrease in H^+ content due to iron corrosion is responsible for a decrease in conductivity, whereas an increase in the contents of other ionic species causes an increase in conductivity.

3. Results and discussion

3.1. Characterization of Pd-mZVI particles

The characterization of the Pd-mZVI particles before reaction is shown in Fig. 1 and Fig S1. On Fig. 1a, it is shown that the smallest particles were spherical, with a diameter of 2-3 µm. Larger particles with a diameter of about 10 µm were also observed (Fig. S1a). On Fig. S1b, the largest particles show the porous structure of the external layer. In addition, EDS analysis reveals that some of the particles have a high carbon content with traces of silicium and phosphorus, which could originate from the biomass used during the bioreductive deposition of palladium nanoparticles (De Windt et al. 2005; Dien et al. 2013).

Fig. 1b shows the patterns of the Pd-mZVI particles. The peaks at 44.7°, 65.1° and 82.3°, respectively, can be indexed to the planes (110), (200) and (211) of Fe cubic crystal structure (JCPDS 06-0696), and the peaks at 40.3°, 46.9° and 68.5°, respectively, correspond to the planes (111), (200) and (220) of face centered cubic crystal structure of Pd (the peak at 82.3° can also be attributed in part to the plane (311)) (JCPDS 46-1043). However, there is no indication of crystalline phases of iron oxide, or only in very small fractions, in contrary to the pattern of nZVI particles for which the diffraction peaks corresponding to magnetite or maghemite were observed (Fig. S2a). Figs 1c, d and e show the XPS spectra of the Pd-mZVI particles. The survey scan from 0 to 1100 eV indicates the presence of Fe, Pd, C, O, N and Si on the surface of the particles (Fig. 2a). As indicated by the low signal intensities between 700 and 730 eV (Fig. 2b), the presence of Fe on the surface of the particles is very limited, in comparison to nZVI particles for which the XPS spectra indicates the presence of metallic iron

205 (Fe^0) and oxidized iron (Fe^{III}) on its surface and near-surface (Fig. S2). The particles present four peaks between
206 332 and 346 eV, named A1, B1, A2 and B2 (Fig. 2c). The two peaks A1 and A2, with binding energies of 335.4
207 and 340.7 eV respectively, match with the $3d_{5/2}$ and $3d_{3/2}$ of metallic Pd (Muftikian et al. 1996; Yan et al. 2010),
208 and the two peaks B1 and B2, with binding energies of 338.1 and 343.4 eV respectively, match with the $3d_{5/2}$ and
209 $3d_{3/2}$ of oxidized Pd (Voogt et al. 1996). The results indicate that, for Pd-mZVI particles, the core is mainly
210 composed of Fe^0, while the external surface of the particles is composed of iron oxides, carbon, silica, and
211 palladium, the latter being required for H^* generation for hydrodechlorination on the surface.

212 *3.2. Investigation of the Pd-mZVI/PLA/H_2O system*

213 Before considering HCA degradation, two experiments were performed without HCA at 25 °C in the presence of
214 600 mg of Pd-mZVI and 850 or 3400 mg of PLA. This was to investigate the influence of PLA on the corrosion
215 kinetics of Pd-mZVI and to understand how to interpret the evolution of pH, ORP and conductivity (Fig. 2).

216 With 850 mg of PLA, the introduction of PLA in solution resulted in an initial drop of pH to 2.65 (Fig. 2a, with
217 pK_a of lactic acid = 3.86 at 20 °C) and a first increase of conductivity to 350 µS cm^{-1} (Fig. 2d). Initially, the ORP
218 values were fixed by the Fe(III)/Fe(II) redox couple (Figs. 2b and c) that result from the initial partial breaking
219 of the iron oxide shell under acidic conditions (Sarathy et al. 2008; Tang et al. 2017a). This agrees with the
220 initial decrease and stabilization of pH as Fe^{3+} acts as a weak Brønsted acid (Shih et al. 2011), as indicated in Eq.
221 5.

$$Fe^{3+} + H_2O \rightarrow Fe(OH)^{2+} + H^+ \qquad \text{(Eq. 5)}$$

222 After 420 minutes, the pH increased from 2.65 to 6.15, and the rate of H^+ consumption is not linear but decreases
223 with time, as shown by the cumulative H^+ consumption (Fig. S3). After an initial decrease, the conductivity
224 stabilized at a minimum value of 195 µS cm^{-1} after 100 min. The decrease in H^+ content was therefore
225 compensated by an increase in other ionic-species contents, especially soluble Fe^{2+} and Fe^{3+}. After that,
226 conductivity slowly increased to 230 µS cm^{-1} at 420 min.

227 According to the Nernst equation of the Fe(III)/Fe(II) redox couple, an increase in Fe^{2+} content resulting from
228 iron corrosion (Eq. 1) causes a decrease in ORP values in the first minutes. Then, ORP drops from positive to
229 negative values (Fig. 2b), which indicates a change in the main redox couple in the system. As shown on Fig. 2c,
230 this change is well correlated with the theoretical evolution of the H^+/H_2 redox couple with pH. Hence, the
231 monitoring of ORP is a good indicator for the formation and accumulation of H_2 in the system. A similar
232 behaviour was observed for the aqueous corrosion of nZVI particles in PLA (Fig. S4), confirming that the

changes in solution chemistry are well related to the particles. However, all phenomena accelerated when using nZVI particles. The pH increased from 2.75 to 6.15 in less than 60 min, resulting in a more rapid initial decrease in both ORP and conductivity. This acceleration is probably related to the difference in specific surface area ($a_{S\ nZVI,\ BET}$ = 15.5 $m^2\ g^{-1}$) and in the cathode/anode ratio. The nZVI particles thus show a much faster corrosion rate than Pd-mZVI particles, the latter having a longer reactive lifetime.

The increase in PLA content from 850 to 3 400 mg led to a decrease in initial pH (Fig. 2a) due to PLA hydrolysis, resulting in an increase in initial conductivity (Fig. 2d). Similar changes of pH and ORP were observed, but with a time delay; the decrease and stabilization of pH values (Fig. 2a) and the fixing of ORP by the Fe(III)/Fe(II) redox couple (Figs. 2b, c) were observed during 40 min. After that, the pH sharply increased reflecting a more rapid decrease in conductivity (Fig. 2d), and the change of ORP from the Fe(III)/Fe(II) to the H^+/H_2 redox couple occurred shortly after. Compared with the experiment conducted with 850 mg of PLA, this evolution of the solution chemistry thus suggests that, despite an initial decrease in pH, iron corrosion is slow from 0 to 40 min, becoming important only after that. The polymeric coating can alter the reactivity of iron-based particles due to (i) the blocking of reactive sites and (ii) the inhibition of mass transfer to the surface due to the formation of trains and loops (Phenrat et al. 2009). Increasing the PLA content results in blocking of the reactive cathodic sites and the creation of an extensive polymer layer on the surface. Iron corrosion thus appears to be initially cathodically controlled by H^+ mass transport to the Pd surface, the effect being more pronounced when the PLA content is increased. Increasing the H^+ content at the interface causes an increase in corrosion rate, resulting in the saturation of Pd and the later recombination of H^* into H_2. A schematic illustration of the main results obtained in this section is proposed on Fig. 3.

Continuous pH, ORP and conductivity measurements allowed monitoring the consumption of H^+, mainly related to iron corrosion, and the production/accumulation of H_2 in the system according to the E-pH diagram.

3.3. Investigation of the Pd-mZVI/PLA/HCA/H_2O system

3.3.1. Effects of Pd-mZVI dosage

The effect of Pd-mZVI dosage was investigated with 150, 375 and 600 mg at 25 °C with 850 mg of PLA and 10 mg L^{-1} of HCA (Fig. 4). It is important to note that the theoretical stoichiometric requirement is 1.42 g Fe^0/g of HCA for its complete reduction to ethane. HCA completely disappears in less than 120 min with 600 mg of Pd-mZVI, while the degradation remains incomplete after 420 min with 150 and 375 mg (Fig. 4a). An increase in Pd-mZVI dosage results in more active sites for H^+ reduction and H^* generation (cathodic sites), as confirmed

by the more rapid increase in pH (Fig. 4b). As shown on Figs. 4d and e, ORP remained fixed by the Fe(III)/Fe(II) redox couple with 150 and 375 mg, while the change from Fe(III)/Fe(II) to H^+/H_2 was observed with 600 mg. This result agrees with the more rapid and greater production of H_2. With 150 and 375 mg of Pd-mZVI, the conductivity decreases during the 420 min of reaction time (Fig. 4f). This decrease is observed during the first 90 min with 600 mg of Pd-mZVI. As H^+ is the major contributor to conductivity under strong acidic conditions, this variation can be explained by a decrease in H^+ content due to iron corrosion.

HCA reduction results in the formation and accumulation of PCE (C_2Cl_4) as the only chlorinated intermediate (Fig. 4c), in agreement with the dihalo-elimination pathway observed in earlier studies with ZVI-based particles (Lien and Zhang 2005; Song and Carraway 2005; Wu et al. 2014). However, our results showed that the initial disappearance of HCA was not directly related to PCE production, as a 10-min shift was observed for PCE production irrespective of the amount of particles. This delay may indicate that HCA degradation initially involves nonreductive sorption on the Pd-mZVI/PLA/H_2O system, which is generally linked to the carbon content on the particle surfaces (Lin and Lo 2005; Velimirovic et al. 2013b). In addition, this induction period could be caused by the absence of active hydrogen species (H^*_{ads}) on the Pd surface, as He et al. (2018) suggested that the dechlorination process on Pd particles requires first their saturation by H^* (formation of palladium hydride) before any dechlorination reaction.

With 600 mg of Pd-mZVI, the change from positive to negative ORP values occurs after 100 min (Fig. 4d) whereas it occurs after only 35 min in the absence of HCA (Fig. 2b), showing that H^* is consumed during dechlorination. This change is observed only when the PCE concentration becomes low, indicating that H^* is the main reductant for both HCA and PCE degradation. However, the degradation mechanism seems different for both compounds. HCA reduction to PCE (Eq. 6) does not involve the addition of hydrogen in the molecule; atomic hydrogen acts therefore only as an electron donor. Even if this result seems to disagree with the increase in pH, it is important to note that iron particles have a very low electron efficiency toward contaminants, i.e. most parts of iron react with water (Schöftner et al. 2015; Fan et al. 2016; Tang et al. 2017b). PCE reduction results in the formation of ethane, ethylene and C_4 compounds (Fig. S6), without accumulation of chlorinated intermediates in solution. This result was confirmed by GC/MS measurements with lower quantitation limits (0.1-1 µg L^{-1} depending on the compound). The production of C_4 compounds indicates that coupling reactions occur during the reaction. Hence, PCE reduction first results in the formation of C_2 surface complexes, with the

loss of chloride ions due to the breaking of C-Cl bonds on the catalyst (Sriwatanapongse et al. 2006; Heck et al. 2008), followed by progressive hydrogenation and/or coupling reactions between C_2 fragments (Eqs. 7-10).

$$CCl_3CCl_3 + 2\,e^- \rightarrow CCl_2 = CCl_2 + 2\,Cl^- \quad \text{(Eq. 6)}$$

$$CCl_2 = CCl_2 \xrightarrow{Pd} C_2^{\ddagger} + 4\,Cl^- \quad \text{(Eq. 7)}$$

$$C_2^{\ddagger} + 6\,H^* \xrightarrow{Pd} C_2H_6 \quad \text{(Eq. 8)}$$

$$C_2^{\ddagger} + 4\,H^* \xrightarrow{Pd} C_2H_4 \quad \text{(Eq. 9)}$$

$$C_2^{\ddagger} + C_2^{\ddagger} \xrightarrow{Pd} C_4^{\ddagger} \quad \text{(Eq. 10)}$$

With 600 mg of Pd-mZVI, the small increase in ORP values (Fig. 4d)—causing a gap in the H^+/H_2 redox couple theoretical values observed after 120 min (Fig. 4e)—is caused by the loss of H_2 during sampling, as ORP remains well fixed by the H^+/H_2 redox couple without opening of the reactor (Fig. 2c). The effect is more pronounced for the penultimate sampling at 330 min because of the decrease in H^+ content and the rate of iron corrosion. The effect is even more pronounced with nZVI particles (Fig. S4), where a decrease in pH is observed after 80 min associated with a progressive increase in ORP every time the reactor is opened. These results indicate a consumption of OH^- and the formation of iron oxy-hydroxides on the surface of nZVI particles such as lepidocrocite γ-FeOOH, because of the possible introduction of dissolved O_2 (Greenlee et al. 2012; Liu et al. 2014a), as well as of ferrihydrite because of the presence of lactate ions (Sabot et al. 2007).

Zero-order, pseudo-first-order and second-order reactions were envisaged for fitting the experimental data. With 150 and 375 mg of Pd-mZVI, none of them resulted in a correct representation of HCA degradation (see Table 1 for the results of pseudo-first-order equations). In these cases, a two-compartment model based on first-order equations (Eq. 11) fits well with the experimental data obtained (Fig. S6), suggesting that two different reaction mechanisms explain the disappearance of HCA (Rodrigues et al. 2017a; Kim et al. 2018).

$$\frac{C}{C_0} = \alpha\, e^{-k_a t} + (1-\alpha)\, e^{-k_c t} \quad \text{(Eq. 11)}$$

where C_0 is the initial pollutant concentration, C is the pollutant concentration at time t (min), k_a and k_c are respectively the rate constants for adsorption and chemical degradation, α represents the weight value for sorption, and 1-α represents the weight value for chemical degradation.

With 600 mg of Pd-mZVI, the production of atomic hydrogen H^* on the Pd surface is more important due to increased H^+ consumption. The rate-determining step then moves progressively from H^* production to hydro-

311 dechlorination by increasing Pd-mZVI dosage, which can explain the validity of the pseudo-first-order model
312 (Eq. 12):

$$\frac{C}{C_0} = e^{-k_{\mathrm{obs}}t} \qquad \text{(Eq. 12)}$$

313 where C is the concentration (mg L^{-1}) at time t (min), C_0 is the initial concentration (mg L^{-1}) and k_{obs} is the rate
314 constant (min^{-1}).

315 In the following section, we focus on the use of 600 mg of Pd-mZVI in order to observe as much variation as
316 possible in the different experimental parameters for a better understanding of the HCA degradation mechanism.

317 *3.3.2. Effects of temperature*

318 The effect of temperature was investigated at 12, 25 and 35 °C with 600 mg of Pd-mZVI, 850 mg of PLA and
319 10 mg L^{-1} of HCA (Fig. 5). As already observed in our previous study (Rodrigues et al. 2017a), the increase in
320 temperature results in a decrease in the initial pH due to a change in the rate of PLA hydrolysis. Results show
321 that HCA degradation is incomplete at 12 °C after 420 min (Fig. 5a). During this period, the pH increases from
322 2.94 to 3.48 (Fig. 5b), and only a decrease in conductivity with time from 390 to 225 µS cm^{-1} is observed
323 (Fig. 5f), indicating that iron corrosion is slow. At 35 °C, the HCA has completely disappeared after about
324 60 min, more rapidly than at 25 °C (Fig. 5a), and PCE accumulates at a lower rate and disappears more rapidly at
325 35 °C (Fig. 5c). In addition to the increase in the number of high-energy collisions and in the mobility of the
326 pollutant, the rise in temperature from 12 to 35 °C increases H^+ consumption (Fig. S3). Direct comparison of the
327 evolution of conductivity is more difficult here as the molar conductivity of each species is different at each
328 temperature, but the results confirm that iron corrosion is more rapid when the temperature increases (Fig. 5f).
329 The constant increase in HCA degradation rate with temperature (Table 1) can then be explained by the more
330 rapid production of atomic hydrogen on the Pd surface (He and Zhao 2008).

331 This agrees with the evolution in ORP values over time. At 12 °C, ORP is stable for 100 min and only a small
332 decrease is observed afterwards (Fig. 5d), indicating an increase in Fe^{2+} content in the solution. The ORP does
333 not decrease to the H^+/H_2 redox couple values because of the slow production of atomic hydrogen and its
334 subsequent reaction with HCA. Conversely, the accumulation of H_2, according to ORP measurements (Fig. 5d),
335 is more rapid at 35 °C than at 25 °C, as both HCA and PCE degradation occur more rapidly. Consequently, the
336 decrease in H^+ consumption under less acidic conditions (pH >5) is observed earlier at 35 °C. After the last
337 opening of the reactor at 330 min, the ORP becomes positive, indicating that the H^+/H_2 redox couple is no longer

the main contributor to the overall ORP value (Figs. 5d and e). Also, the small decrease in pH observed could indicate an OH^- consumption related to the formation of iron oxy-hydroxides on the particle surfaces. Thus, even if the temperature increase is favourable for HCA degradation, the reactive lifetime of the particles and the electron efficiency are strongly impacted. We thus focused on the use of T = 25 °C for the subsequent experiments.

Considering the pseudo-first-order model, the Arrhenius equation was used for establishing the relation between the rate constant and the temperature (Eq. 13).

$$\ln k_{\mathrm{obs}} = \ln A - \frac{E_a}{RT} \quad \text{(Eq. 13)}$$

where k_{obs} is the constant rate (min^{-1}), A is the pre-exponential factor (min^{-1}), E_a is the activation energy (J mol^{-1}), R is the universal gas constant and T is the absolute temperature (K). An almost equivalent relationship, the Eyring equation, can be used by following the transition state theory (Eq. 14).

$$k_{\mathrm{obs}} = \frac{k_{\mathrm{B}} T}{h} \exp\left(\frac{-\Delta^{\ddagger} G^{\circ}}{RT}\right) \quad \text{(Eq. 14)}$$

where k_B is the Boltzmann constant (1.381 10^{-23} J K^{-1}), h is the Planck constant (6.626 10^{-34} J s) and $\Delta^{\ddagger}G°$ is the Gibbs energy of activation (J mol^{-1}). The relation can be linearized as Eq. 15:

$$\ln\left(\frac{k_{\mathrm{obs}}}{T}\right) = \frac{-\Delta^{\ddagger} H^{\circ}}{R} \cdot \frac{1}{T} + \ln\left(\frac{k_{\mathrm{B}}}{h}\right) + \frac{\Delta^{\ddagger} S^{\circ}}{R} \quad \text{(Eq. 15)}$$

where $\Delta^{\ddagger}H°$ is the standard enthalpy of activation (J mol^{-1}) and $\Delta^{\ddagger}S°$ is the standard entropy of activation (J $mol^{-1}{\cdot}K^{-1}$).

Results obtained from the Arrhenius plot are Ea = 106.5 kJ mol^{-1} and A = 1.21 10^{17} min^{-1} (R^2 = 0.982, Fig. S8a). The elevated activation energy indicates that, with these experimental parameters, the overall reaction is controlled by the reaction on the particle surfaces (Pilling and Seakins 1995). Results obtained from the Eyring plot are $\Delta^{\ddagger}H°$ = 104.0 kJ mol^{-1} and $\Delta^{\ddagger}S°$ = 39.8 J mol^{-1} K^{-1} (R^2 = 0.981, Fig. S8b). The positive value for the activation entropy indicates that the reaction is favourable and that the activated complex is loosely bound on the surface of the particles, which agrees with the formation and desorption of PCE as a reaction intermediate. Based on previous studies (Butler and Hayes 1998; Patterson et al. 2001; Song and Carraway 2005; Huang et al. 2012; Pizarro et al. 2018), the activated complex is suspected to be the pentachloroethyl radical (Eqs. 16-17).

$$C_2Cl_6 + e^- \rightarrow {}^{\bullet}C_2Cl_5 + Cl^- \quad \text{(Eq. 16)}$$

$${}^{\bullet}C_2Cl_5 + e^- \rightarrow C_2Cl_4 + Cl^- \quad \text{(Eq. 17)}$$

3.3.3. Effects of HCA initial concentration

The effect of the initial concentration was investigated at three HCA initial concentrations—5, 10 and 20 mg L^{-1}—at 25 °C with 600 mg of Pd-mZVI and 850 mg of PLA (Fig. 6). A change in initial concentration of the substrate has no influence on the degradation pathways, with the production of PCE and its subsequent reduction to ethane, ethylene and C_4 compounds (Fig. S9). HCA degradation-rate constants are very similar when the initial concentration increases from 5 mg L^{-1} (k_{obs} = 0.036 min^{-1}) to 10 mg L^{-1} (k_{obs} = 0.035 min^{-1}, see Table 1). As the evolution of H^+ content is quite different at both concentrations (Figs. 6b and S2), the rate-determining step cannot be attributed to H^* production, but rather to HCA dechlorination.

An increase in HCA content to 20 mg L^{-1} results in a decrease in the degradation rate constant (k_{obs} = 0.010 min^{-1}), and PCE accumulates over a longer time, but in a similar proportion as obtained with lower initial concentrations (Fig. 6c). As indicated by the pH evolution (Fig. 6b) and cumulative H^+ consumption (Fig. S3), the production of H^* is less rapid with 20 mg L^{-1}, whereas the degradation requires twice as much atomic hydrogen. As observed in Figs. 6d and e, the ORP value remains positive and is not fixed by the H^+/H_2 redox couple during the 420 min of the experiment. As shown on Fig. S10, the drop in ORP values is observed only after the complete hydrodechlorination of PCE. So, as long as dechlorination occurs, the most important fraction of H^*_{ads} available on Pd is consumed, which prevents its recombination into H_2 and its subsequent desorption. Therefore, even if the degradation rate constant is lower, a low iron/pollutant ratio will limit the loss of active hydrogen species. This result is comparable to that obtained by decreasing the amount of Pd-mZVI, where a similar evolution of conductivity with time is observed (Fig. 6f). Hence, for higher HCA initial concentrations (>20 mg L^{-1}) with 600 mg of Pd-mZVI, the reaction may be limited by the production of H^* and not by surface-reaction kinetics.

In the following section, we thus focus on the use of 10 mg L^{-1} as the initial HCA concentration.

3.3.4. Effects of PLA content

The effect of the PLA content was investigated for three initial contents—850, 1700 and 3400 mg—at 25 °C with 600 mg Pd-mZVI and 10 mg L^{-1} HCA (Fig. 7). The increase in PLA content results in a decrease in HCA degradation rate constants, from 0.035 min^{-1} with 850 mg to 0.025 min^{-1} at 3400 mg (Table 1), in agreement with

386 the later production and accumulation of PCE (Fig. 7c). With 3400 mg, more than 40% of HCA disappears in the
387 first 10 min, which indicates a more important phase transfer from water to PLA (sorption). As no PCE
388 production is observed during this time, HCA accumulates near the surface of the particles. Compared to the
389 experiment run in the Pd-mZVI/PLA/H_2O system (Fig. 2), the evolution of pH, ORP and conductivity follows
390 the same qualitative trend (Figs. 7b, d and f), although H^+ consumption is less important in the first minutes
391 (Fig. S3) and the change from a Fe(III)/Fe(II) to a H^+/H_2 redox couple occurs much later.

392 In the Pd-mZVI/PLA/H_2O system, the reductive dechlorination process requires an intimate contact between
393 pollutant and particle surface. However, as mentioned before, the increase in polymeric coating can result in a
394 high coverage rate of the particles (site blocking) and the development of an extended layer composed of loops
395 and tails (Zhu et al. 2008; Phenrat et al. 2009; Bhattacharjee et al. 2016; Louie et al. 2016). With 1700 mg of
396 PLA, the lower HCA rate constant can be attributed to higher number of sites blocked by the polymeric coating
397 and to a low production of atomic hydrogen in the first minutes. After the initial decrease and stabilization of pH
398 (Fig. 7b), the strong acidic conditions accelerate the rate of H^+ consumption (Fig. S3), which results in a more
399 rapid production of H^*. As a consequence, PCE degradation occurs rapidly. With 3400 mg of PLA, the
400 development of loops and tails on the particle surfaces will impede HCA mass transport to the surface of the
401 particles, the accumulation of HCA in turn impeding H^+ mass transport, which explains the decrease in
402 degradation rate. In addition, the accumulation of H_2 bubbles around the particles can result in the covering of
403 reactive sites and the deactivation of the catalyst (Graham and Jovanovic 1999; Wang et al. 2009), leading to a
404 further decrease in the degradation rate (Huang et al. 2016).

405 Even if the degradation rates decrease with increasing PLA content, the reactive lifetime of the particles is
406 extended thanks to the formation of iron lactate complexes and the maintenance of acidic conditions, which
407 prevent the rapid formation of any passive layer on the surface of the particles (Rodrigues et al. 2017a) as Fe^{3+}
408 and Fe^{2+} are more soluble under acidic conditions, and thus the rapid enclosure of Pd (Yan et al. 2010; Ling and
409 Zhang 2014).

410 As shown in the previous experiments, for a given initial HCA concentration, an increase in Pd-mZVI dosage
411 causes an increase in the HCA degradation rate, but a major part of the H^* will be combined as H_2, rendering it
412 unavailable for degradation. Therefore, it appears necessary to seek a compromise between HCA degradation
413 rate and electron efficiency. A 15:85 mass ratio of Pd-mZVI in PLA appears to be an optimal condition that

allows a rapid initial disappearance of the pollutant, a more controlled reactivity and the maintenance of acidic conditions, extending the reactive lifetime of the particles and preventing the formation of passive precipitates.

3.4. HCA dechlorination mechanism

Figure 8 shows a summary of the main conclusions of the dechlorination mechanism. The introduction in water of a suspension of Pd-mZVI in PLA results in the partial breaking up of the initial shell (Sarathy et al. 2008; Tang et al. 2017a); Fe^0 oxidizes to Fe^{2+}, and the resulting electrons flow from the iron core to Pd that acts as the main cathodic site ($E^0_{Pd} > E^0_{FeOx} > E^0_{Fe}$). On the Pd surface, which is a good catalyst for hydrogenation, H^+ is reduced to atomic hydrogen H^* (Volmer step), accumulating as palladium hydride (Pd-H) and as H^*_{ads}. Finally, the reaction of H^+ with H^*_{ads} (Heyrovsky step), or the combination of two H^*_{ads} (Tafel step), will result in the desorption of H_2 to the bulk solution (Fig. 3).

In the presence of HCA, the first step is mass transfer of HCA from bulk to suspension of the Pd-mZVI/PLA system. As both HCA and PLA are hydrophobic, the initial HCA disappearance is attributed to nonreductive sorption, in agreement with the absence of PCE production and the increase in initial disappearance when increasing the PLA content. The second step is the surface reaction of HCA with H^*, which results in the production and accumulation of PCE as a chlorinated by-product. The absence of other chlorinated intermediates and the production of C_4 compounds suggest that PCE undergoes rapid dechlorination, because of the breaking of C-Cl bonds on the Pd surface (Sriwatanapongse et al. 2006; Heck et al. 2008) and the formation of $C_2^{\ddagger}$ surface complexes. The third step is the progressive hydrogenation of $C_2^{\ddagger}$ into C_2 compounds, or a coupling reaction between two surface complexes into $C_4^{\ddagger}$ and its progressive hydrogenation to C_4 compounds. The last steps are the desorption of the products from the surface of the particles, and their transfer to the bulk solution (Fig. 8).

3.5. Implications for environmental application

In addition to proposing a degradation mechanism, our study allows defining some perspectives for practical applications. The laboratory results suggest that small (≈600 mg for $[HCA]_0$ = 5-20 mg L^{-1}) amounts of Pd-mZVI in PLA are sufficient for a rapid and complete pollution degradation. The use of low doses of iron particles will limit the loss of ZVI due to its spontaneous corrosion in water, as well as reducing its inhibition effects on the microbial community for *in situ* remediation (Velimirovic et al. 2015). Even if an increase in PLA content results in more acidic conditions, the effect may be less pronounced under field conditions depending on the natural buffering capacity of the aquifer. In addition, as indicated above, iron corrosion progressively results in an increase of pH to near-neutral conditions, more favourable to the growth and activity of organohalide-

443 respiring bacteria, e.g. *Dehalococcoides* strains, for biological reductive dechlorination, even if a pH decrease
444 will affect the ability of the culture to dechlorinate (Yang et al. 2017a, b). The monitoring of pH thus is a great
445 tool for evaluating the operating conditions for both abiotic and biotic reductive processes.

446 Interpretation of the ORP evolution should be more difficult in the field than in laboratory experiments, because
447 of the many redox couples and bacteria in groundwater that contribute to the overall (mixed potential) ORP
448 value (Hunting and Kampfraath 2013; Shi et al. 2015). Measuring ORP will nevertheless provide insight into the
449 creation of reductive conditions due to H_2 production. In addition, the impact on ORP values of opening the
450 reactor could mirror the influence of sampling from observation wells in the field, as ORP values are known to
451 have a harmful effect on iron reactivity, and on the presence and activity of organohalide-respiring bacteria
452 (Adrian and Löffler 2016). Finally, conductivity measurements should give indications on the ionic strength of
453 groundwater. The overall data acquired during this study have shown the interest of implementing a complete
454 multi-parametric device for the monitoring of reductive dechlorination processes in the field.

455 **4. Conclusion**

456 We investigated the mechanism of HCA degradation by a suspension of Pd-mZVI particles in PLA, using
457 indirect continuous monitoring of iron corrosion by means of measuring pH, ORP and conductivity. HCA
458 dechlorination involves the formation and accumulation of PCE as an intermediate compound, before its
459 subsequent reduction to non-chlorinated C_2 and C_4 compounds. The increase in Pd-mZVI dosage results in an
460 increased HCA degradation rate due to a greater production of atomic hydrogen H^*. With 600 mg of Pd-mZVI
461 particles, a temperature increase is favourable to HCA degradation as the production of H^* is accelerated, but at
462 the expense of the reactive lifetime of the particles. Increasing the initial HCA concentration to 20 mg L^{-1} leads
463 to a decrease in the degradation rate constant. Finally, an increase in PLA content decreases the global
464 degradation rate due to an enhanced contact between HCA and the particle surfaces that decreases the production
465 of H^*, but the maintaining of acidic conditions can prevent the rapid formation of any passive precipitates. Our
466 results indicate that the HCA degradation mechanism includes mass transfer, nonreductive sorption, surface
467 reaction with H^* and desorption of the product. Combined with gas chromatography, the continuous monitoring
468 of physical and chemical parameters of the bulk solution was proven to be a powerful tool in laboratory
469 experiments for the indirect investigation of dechlorination mechanisms in the Pd-mZVI/PLA/H_2O system.

Appendix A. Supplementary data

Supplementary data are associated with this article.

Declaration of interest

None

Acknowledgements

This work was supported by the French Environment and Energy Management Agency (ADEME) and the French Geological Survey (BRGM) within the framework of the AMI SILPHES project coordinated by David Cazaux (Inovyn Tavaux). The authors acknowledge Benoit Castermans (Biorem Engineering) for providing Pd-mZVI particles and PLA, Nicolas Maubec (BRGM) for performing XRD analyses, and Christian Perruchot and Philippe Decorse (ITODYS laboratory, Université Paris Diderot) for performing XPS analyses. Romain Rodrigues thanks Chérif Morcos for fruitful discussions. The authors thank the anonymous reviewers for their helpful comments and suggestions. H.M. Kluijver edited the English language of the final MS.

References

Adrian L, Löffler FE (2016) Organohalide-Respiring Bacteria. Springer, Berlin, Heidelberg

Aulenta F, Fuoco M, Canosa A, Papini MP, Majone M (2008) Use of poly-β-hydroxy-butyrate as a slow-release electron donor for the microbial reductive dechlorination of TCE. Water Sci Technol 57:921. doi: 10.2166/wst.2008.073

Bae S, Collins RN, Waite TD, Hanna K (2018) Advances in surface passivation of nanoscale zerovalent iron (NZVI): A critical review. Environ Sci Technol acs.est.8b01734. doi: 10.1021/acs.est.8b01734

Bae S, Hanna K (2015) Reactivity of nanoscale zero-valent iron in unbuffered systems: Effect of pH and Fe(II) dissolution. Environ Sci Technol 49:10536–10543. doi: 10.1021/acs.est.5b01298

Baer DR, Amonette JE, Engelhard MH, Gaspar DJ, Karakoti AS, Kuchibhatla S, Nachimuthu P, Nurmi JT, Qiang Y, Sarathy V, Seal S, Sharma A, Tratnyek PG, Wang C-M (2008) Characterization challenges for nanomaterials. Surf Interface Anal 40:529–537. doi: 10.1002/sia.2726

Baric M, Majone M, Beccari M, Papini MP (2012) Coupling of polyhydroxybutyrate (PHB) and zero valent iron (ZVI) for enhanced treatment of chlorinated ethanes in permeable reactive barriers (PRBs). Chem Eng J

195–196:22–30. doi: 10.1016/j.cej.2012.04.026

Bhattacharjee S, Basnet M, Tufenkji N, Ghoshal S (2016) Effects of rhamnolipid and carboxymethylcellulose coatings on reactivity of palladium-doped nanoscale zerovalent iron particles. Environ Sci Technol 50:1812–1820. doi: 10.1021/acs.est.5b05074

Bruton TA, Pycke BFG, Halden RU (2015) Effect of nanoscale zero-valent iron treatment on biological reductive dechlorination: A review of current understanding and research needs. Crit Rev Environ Sci Technol 45:1148–1175. doi: 10.1080/10643389.2014.924185

Butler EC, Hayes KF (1998) Effects of solution composition and pH on the reductive dechlorination of hexachloroethane by iron sulfide. Environ Sci Technol 32:1276–1284. doi: 10.1021/es9706864

Chaplin BP, Reinhard M, Schneider WF, Schüth C, Shapley JR, Strathmann TJ, Werth CJ (2012) Critical review of Pd-based catalytic treatment of priority contaminants in water. Environ Sci Technol 46:3655–3670. doi: 10.1021/es204087q

Chronopoulou L, Palocci C, Valentino F, Pettiti I, Wacławek S, Černík M, Papini MP (2016) Stabilization of iron (micro)particles with polyhydroxybutyrate for in situ remediation applications. Appl Sci 6:417. doi: 10.3390/app6120417

Comba S, Di Molfetta A, Sethi R (2011) A comparison between field applications of nano-, micro-, and millimetric zero-valent iron for the remediation of contaminated aquifers. Water, Air, Soil Pollut 215:595–607. doi: 10.1007/s11270-010-0502-1

Crane RA, Scott TB (2012) Nanoscale Zero-Valent Iron: Future Prospects for an Emerging Water Treatment Technology. J Hazard Mater 211:112–125. doi: 10.1016/j.jhazmat.2011.11.073

De Windt W, Aelterman P, Verstraete W (2005) Bioreductive deposition of palladium (0) nanoparticles on Shewanella oneidensis with catalytic activity towards reductive dechlorination of polychlorinated biphenyls. Environ Microbiol 7:314–325. doi: 10.1111/j.1462-2920.2005.00696.x

Dien NT, De Windt W, Buekens A, Chang MB (2013) Application of bimetallic iron (BioCAT slurry) for pentachlorophenol removal from sandy soil. J Hazard Mater 252:83–90. doi: 10.1016/j.jhazmat.2013.02.029

522 Elliott DW, Zhang W (2001) Field assessment of nanoscale bimetallic particles for groundwater treatment.
523 Environ Sci Technol 35:4922–4926. doi: 10.1021/es0108584

524 Fan D, O'Carroll DM, Elliott DW, Xiong Z, Tratnyek PG, Johnson RL, Garcia AN (2016) Selectivity of nano
525 zerovalent iron in in situ chemical reduction: Challenges and improvements. Remediat J 26:27–40. doi:
526 10.1002/rem.21481

527 Fang L, Xu C, Zhang W, Huang L-Z (2018) The important role of polyvinylpyrrolidone and Cu on enhancing
528 dechlorination of 2,4-dichlorophenol by Cu/Fe nanoparticles: Performance and mechanism study. Appl
529 Surf Sci 435:55–64. doi: 10.1016/j.apsusc.2017.11.084

530 Filip J, Karlický F, Marušák Z, Lazar P, Černík M, Otyepka M, Zbořil R (2014) Anaerobic reaction of nanoscale
531 zerovalent iron with water: Mechanism and kinetics. J Phys Chem C 118:13817–13825. doi:
532 10.1021/jp501846f

533 Fu F, Dionysiou DD, Liu H (2014) The use of zero-valent iron for groundwater remediation and wastewater
534 treatment: A review. J Hazard Mater 267:194–205. doi: 10.1016/j.jhazmat.2013.12.062

535 Gillham RW, O'Hannesin SF (1994) Enhanced degradation of halogenated aliphatics by zero-valent iron.
536 Ground Water 32:958–967. doi: 10.1111/j.1745-6584.1994.tb00935.x

537 Graham LJ, Jovanovic G (1999) Dechlorination of p-chlorophenol on a Pd/Fe catalyst in a magnetically
538 stabilized fluidized bed; Implications for sludge and liquid remediation. Chem Eng Sci 54:3085–3093. doi:
539 10.1016/S0009-2509(98)00393-5

540 Greenlee LF, Torrey JD, Amaro RL, Shaw JM (2012) Kinetics of zero valent iron nanoparticle oxidation in
541 oxygenated water. Environ Sci Technol 46:12913–12920. doi: 10.1021/es303037k

542 Grieger KD, Fjordbøge A, Hartmann NB, Eriksson E, Bjerg PL, Baun A (2010) Environmental benefits and
543 risks of zero-valent iron nanoparticles (nZVI) for in situ remediation: Risk mitigation or trade-off? J
544 Contam Hydrol 118:165–183. doi: 10.1016/j.jconhyd.2010.07.011

545 Grittini C, Malcomson M, Fernando Q, Korte N (1995) Rapid dechlorination of polychlorinated biphenyls on the
546 surface of a Pd/Fe bimetallic system. Environ Sci Technol 29:2898–2900. doi: 10.1021/es00011a029

547 Han J, Xin J, Zheng X, Kolditz O, Shao H (2016) Remediation of trichloroethylene-contaminated groundwater

548 by three modifier-coated microscale zero-valent iron. Environ Sci Pollut Res 23:14442–14450. doi:
549 10.1007/s11356-016-6368-z

550 He F, Li Z, Shi S, Xu W, Sheng H, Gu Y, Jiang Y, Xi B (2018) Dechlorination of excess trichloroethene by
551 bimetallic and sulfidated nanoscale zero-valent iron. Environ Sci Technol 52:8627–8637. doi:
552 10.1021/acs.est.8B01735

553 He F, Zhao D (2008) Hydrodechlorination of trichloroethene using stabilized Fe-Pd nanoparticles: Reaction
554 mechanism and effects of stabilizers, catalysts and reaction conditions. Appl Catal B Environ 84:533–540.
555 doi: 10.1016/j.apcatb.2008.05.008

556 He F, Zhao D, Liu J, Roberts CB (2007) Stabilization of Fe−Pd nanoparticles with sodium carboxymethyl
557 cellulose for enhanced transport and dechlorination of trichloroethylene in soil and groundwater. Ind Eng
558 Chem Res 46:29–34. doi: 10.1021/ie0610896

559 He F, Zhao D, Paul C (2010) Field assessment of carboxymethyl cellulose stabilized iron nanoparticles for in
560 situ destruction of chlorinated solvents in source zones. Water Res 44:2360–2370. doi:
561 10.1016/j.watres.2009.12.041

562 Heck KN, Janesko BG, Scuseria GE, Halas NJ, Wong MS (2008) Observing metal-catalyzed chemical reactions
563 in situ using surface-enhanced raman spectroscopy on Pd-Au nanoshells. J Am Chem Soc 130:16592–
564 16600. doi: 10.1021/ja803556k

565 Herrero J, Puigserver D, Nijenhuis I, Kuntze K, Carmona JM (2019) Combined use of ISCR and biostimulation
566 techniques in incomplete processes of reductive dehalogenation of chlorinated solvents. Sci Total Environ
567 648:819–829. doi: 10.1016/j.scitotenv.2018.08.184

568 Howard PH (1989) Handbook of Environmental Fate and Exposure Data for Organic Chemicals. CRC Press

569 Huang B, Isse AA, Durante C, Wei C, Gennaro A (2012) Electrocatalytic properties of transition metals toward
570 reductive dechlorination of polychloroethanes. Electrochim Acta 70:50–61. doi:
571 10.1016/jelectacta.2012.03.009

572 Huang B, Qian W, Yu C, Wang T, Zeng G, Lei C (2016) Effective catalytic hydrodechlorination of o-, p- and m-
573 chloronitrobenzene over Ni/Fe nanoparticles: Effects of experimental parameter and molecule structure on
574 the reduction kinetics and mechanisms. Chem Eng J 306:607–618. doi: 10.1016/j.cej.2016.07.109

575 Hunting ER, Kampfraath AA (2013) Contribution of bacteria to redox potential (Eh) measurements in
576 sediments. Int J Environ Sci Technol 10:55–62. doi: 10.1007/s13762-012-0080-4

577 Jiang G, Lan M, Zhang Z, Lv X, Lou Z, Xu X, Dong F, Zhang S (2017) Identification of active hydrogen species
578 on palladium nanoparticles for an enhanced electrocatalytic hydrodechlorination of 2,4-dichlorophenol in
579 water. Environ Sci Technol 51:7599–7605. doi: 10.1021/acs.est.7b01128

580 Jiang G, Wang K, Li J, Fu W, Zhang Z, Johnson G, Lv X, Zhang Y, Zhang S, Dong F (2018) Electrocatalytic
581 hydrodechlorination of 2,4-dichlorophenol over palladium nanoparticles and its pH-mediated tug-of-war
582 with hydrogen evolution. Chem Eng J 348:26–34. doi: 10.1016/j.cej.2018.04.173

583 Kaifas D, Malleret L, Kumar N, Fétimi W, Claeys-Bruno M, Sergent M, Doumenq P (2014) Assessment of
584 potential positive effects of nZVI surface modification and concentration levels on TCE dechlorination in
585 the presence of competing strong oxidants, using an experimental design. Sci Total Environ 481:335–342.
586 doi: 10.1016/j.scitotenv.2014.02.04

587 Kim C, Ahn J-Y, Kim TY, Shin WS, Hwang I (2018) Activation of persulfate by nanosized zero-valent iron
588 (NZVI): Mechanisms and transformation products of NZVI. Environ Sci Technol 52:3625–3633. doi:
589 10.1021/acs.est.7b05847

590 Kim YH, Carraway ER (2003) Reductive dechlorination of TCE by zero valent bimetals. Environ Technol
591 24:69–75. doi: 10.1080/09593330309385537

592 Kocur CM, Chowdhury AI, Sakulchaicharoen N, Boparai HK, Weber KP, Sharma P, Krol MM, Austrins L,
593 Peace C, Sleep BE, O'Carroll DM (2014) Characterization of nZVI mobility in a field scale test. Environ
594 Sci Technol 48:2862–2869. doi: 10.1021/es4044209

595 Kocur CMD, Lomheim L, Molenda O, Weber KP, Austrins LM, Sleep BE, Boparai HK, Edwards EA, O'Carroll
596 DM (2016) Long-term field study of microbial community and dechlorinating activity following
597 carboxymethyl cellulose-stabilized nanoscale zero-valent iron injection. Environ Sci Technol 50:7658–
598 7670. doi: 10.1021/acs.est.6b01745

599 Koenig JC, Boparai HK, Lee MJ, O'Carroll DM, Barnes RJ, Manefield MJ (2016) Particles and enzymes:
600 Combining nanoscale zero valent iron and organochlorine respiring bacteria for the detoxification of
601 chloroethane mixtures. J Hazard Mater 308:106–112. doi: 10.1016/j.jhazmat.2015.12.036

602 Kumar N, Auffan M, Gattacceca J, Rose J, Olivi L, Borschneck D, Kvapil P, Jublot M, Kaifas D, Malleret L,
603 Doumenq P, Bottero J-Y (2014) Molecular insights of oxidation process of iron nanoparticles:
604 Spectroscopic, magnetic, and microscopic evidence. Environ Sci Technol 48:13888–13894. doi:
605 10.1021/es503154q

606 Kumar N, Labille J, Bossa N, Auffan M, Doumenq P, Rose J, Bottero J-Y (2017) Enhanced transportability of
607 zero valent iron nanoparticles in aquifer sediments: Surface modifications, reactivity, and particle traveling
608 distances. Environ Sci Pollut Res 24:9269–9277. doi: 10.1007/s11356-017-8597-1

609 Lee C, Kim JY, Lee W Il, Nelson KL, Yoon J, Sedlak DL (2008) Bactericidal effect of zero-valent iron
610 nanoparticles on Escherichia coli. Environ Sci Technol 42:4927–4933. doi: 10.1021/es800408u

611 Lien H-L, Zhang W (2007) Nanoscale Pd/Fe bimetallic particles: Catalytic effects of palladium on
612 hydrodechlorination. Appl Catal B Environ 77:110–116. doi: 10.1016/j.apcatb.2007.07.014

613 Lien H-L, Zhang W (1999) Transformation of chlorinated methanes by nanoscale iron particles. J Environ Eng
614 125:1042–1047. doi: 10.1061/(ASCE)0733-9372(1999)125:11(1042)

615 Lien H-L, Zhang W (2005) Hydrodechlorination of chlorinated ethanes by nanoscale Pd/Fe bimetallic particles.
616 J Environ Eng 131:4–10. doi: 10.1061/(ASCE)0733-9372(2005)131:1(4)

617 Lin CJ, Lo S-L (2005) Effects of iron surface pretreatment on sorption and reduction kinetics of
618 trichloroethylene in a closed batch system. Water Res 39:1037–1046. doi: 10.1016/j.watres.2004.06.035

619 Ling L, Huang X, Li M, Zhang W (2017) Mapping the reactions in a single zero-valent iron nanoparticle.
620 Environ Sci Technol 51:14293–14300. doi: 10.1021/acs.est.7b02233

621 Ling L, Zhang W (2014) Structures of Pd–Fe(0) Bimetallic nanoparticles near 0.1 nm resolution. RSC Adv
622 4:33861. doi: 10.1039/C4RA04311A

623 Liu A, Liu J, Han J, Zhang W (2017) Evolution of nanoscale zero-valent iron (nZVI) in water: Microscopic and
624 spectroscopic evidence on the formation of nano- and micro-structured iron oxides. J Hazard Mater
625 322:129–135. doi: 10.1016/j.jhazmat.2015.12.070

626 Liu A, Liu J, Pan B, Zhang W (2014a) Formation of lepidocrocite (γ-FeOOH) from oxidation of nanoscale zero-
627 valent iron (nZVI) in oxygenated water. RSC Adv 4:57377–57382. doi: 10.1039/C4RA08988J

628 Liu A, Zhang W (2014) Fine structural features of nanoscale zero-valent iron characterized by spherical
629 aberration corrected scanning transmission electron microscopy (Cs-STEM). Analyst 139:4512–4518. doi:
630 10.1039/C4AN00679H

631 Liu R, Zhao H, Zhao X, He Z, Lai Y, Shan W, Bekana D, Li G, Liu J (2018) Defect sites in ultrathin Pd
632 nanowires facilitate the highly efficient electrochemical hydrodechlorination of pollutants by H*ads.
633 Environ Sci Technol 52:9992–10002. doi: 10.1021/acs.est.8b02740

634 Liu W-J, Qian T-T, Jiang H (2014b) Bimetallic Fe nanoparticles: Recent advances in synthesis and application
635 in catalytic elimination of environmental pollutants. Chem Eng J 236:448–463. doi:
636 10.1016/j.cej.2013.10.062

637 Liu Y, Lowry G V. (2006) Effect of particle age (Fe0 content) and solution pH on NZVI reactivity: H2 evolution
638 and TCE dechlorination. Environ Sci Technol 40:6085–6090. doi: 10.1021/es060685o

639 Louie SM, Tilton RD, Lowry G V (2016) Critical review: Impacts of macromolecular coatings on critical
640 physicochemical processes controlling environmental fate of nanomaterials. Environ Sci Nano 3:283–310.
641 doi: 10.1039/C5EN00104H

642 Lowry G V, Reinhard M (1999) Hydrodehalogenation of 1- to 3-carbon halogenated organic compounds in
643 water using a palladium catalyst and hydrogen gas. Environ Sci Technol 33:1905–1910. doi:
644 10.1021/es980963m

645 Martin JE, Herzing AA, Yan W, Li X, Koel BE, Kiely CJ, Zhang W (2008) Determination of the oxide layer
646 thickness in core−shell zerovalent iron nanoparticles. Langmuir 24:4329–4334. doi: 10.1021/la703689K

647 Mu Y, Jia F, Ai Z, Zhang L (2017) Iron oxide shell mediated environmental remediation properties of nano zero-
648 valent iron. Environ Sci Nano 4:27–45. doi: 10.1039/C6EN00398B

649 Muftikian R, Nebesny K, Fernando Q, Korte N (1996) X-ray photoelectron spectra of the palladium−iron
650 bimetallic surface used for the rapid dechlorination of chlorinated organic environmental contaminants.
651 Environ Sci Technol 30:3593–3596. doi: 10.1021/es960289D

652 Noubactep C (2008) A critical review on the process of contaminant removal in Fe0-H2O systems. Environ
653 Technol 29:909–920. doi: 10.1080/09593330802131602

654 Noubactep C, Caré S, Crane R (2012) Nanoscale metallic iron for environmental remediation: Prospects and
655 limitations. Water Air Soil Pollut 223:1363–1382. doi: 10.1007/s11270-011-0951-1

656 Nurmi JT, Tratnyek PG, Sarathy V, Baer DR, Amonette JE, Pecher K, Wang C, Linehan JC, Matson DW, Penn
657 RL, Driessen MD (2005) Characterization and properties of metallic iron nanoparticles: Spectroscopy,
658 electrochemistry, and kinetics. Environ Sci Technol 39:1221–1230. doi: 10.1021/es049190U

659 O'Hannesin SF, Gillham RW (1998) Long-term performance of an in situ "iron wall" for remediation of VOCs.
660 Ground Water 36:164–170. doi: 10.1111/j.1745-6584.1998.tb01077.x

661 O 'Carroll D, Sleep B, Krol M, Boparai H, Kocur C (2013) Nanoscale zero valent iron and bimetallic particles
662 for contaminated site remediation. Adv Water Resour 51:104–122. doi: 10.1016/j.advwatres.2012.02.005

663 Papaderakis A, Tsiplakides D, Balomenou S, Sotiropoulos S (2017) Probing the hydrogen adsorption affinity of
664 Pt and Ir by surface interrogation scanning electrochemical microscopy (SI-SECM). Electrochem Commun
665 83:77–80. doi: 10.1016/j.elecom.2017.09.003

666 Patterson E V., Cramer CJ, Truhlar DG (2001) Reductive dechlorination of hexachloroethane in the
667 environment: Mechanistic studies via computational electrochemistry. J Am Chem Soc 123:2025–2031.
668 doi: 10.1021/ja0035349

669 Phenrat T, Liu Y, Tilton RD, Lowry G V (2009) Adsorbed polyelectrolyte coatings decrease Fe(0) nanoparticle
670 reactivity with TCE in water: Conceptual model and mechanisms. Environ Sci Technol 43:1507–14. doi:
671 10.1021/es802187d

672 Phenrat T, Saleh N, Sirk K, Kim H-J, Tilton RD, Lowry G V. (2008) Stabilization of aqueous nanoscale
673 zerovalent iron dispersions by anionic polyelectrolytes: Adsorbed anionic polyelectrolyte layer properties
674 and their effect on aggregation and sedimentation. J Nanoparticle Res 10:795–814. doi: 10.1007/s11051-
675 007-9315-6

676 Pierro L, Matturro B, Rossetti S, Sagliaschi M, Sucato S, Alesi E, Bartsch E, Arjmand F, Papini MP (2017)
677 Polyhydroxyalkanoate as a slow-release carbon source for in situ bioremediation of contaminated aquifers:
678 from laboratory investigation to pilot-scale testing in the field. N Biotechnol 37:60–68. doi:
679 10.1016/j.nbt.2016.11.004

680 Pilling MJ, Seakins PW (1995) Reaction Kinetics. Oxford University Press, New York, NY, USA.

Pizarro S, Araya M, Delgadillo A (2018) Hexachloroethane reduction catalyzed by cobaloximes. Effect of the substituents on the equatorial ligands. Polyhedron 141:94–99. doi: 10.1016/j.poly.2017.11.005

Reddy AVB, Yusop Z, Jaafar J, Reddy YVM, Aris A Bin, Majid ZA, Talib J, Madhavi G (2016) Recent progress on Fe-based nanoparticles: Synthesis, properties, characterization and environmental applications. J Environ Chem Eng 4:3537–3553. doi: 10.1016/j.jece.2016.07.035

Reddy KR, Khodadoust AP, Darko-Kagya K (2014) Transport and reactivity of lactate-modified nanoscale iron particles for remediation of DNT in subsurface soils. J Environ Eng 140:04014042. doi: 10.1061/(ASCE)EE.1943-7870.0000870

Rodrigues R, Betelu S, Colombano S, Masselot G, Tzedakis T, Ignatiadis I (2017a) Reductive dechlorination of hexachlorobutadiene by a Pd/Fe microparticle suspension in dissolved lactic acid polymers: Degradation mechanism and kinetics. Ind Eng Chem Res 56:12092–12100. doi: 10.1021/acs.iecr.7b03012

Rodrigues R, Betelu S, Colombano S, Masselot G, Tzedakis T, Ignatiadis I (2017b) Influence of temperature and surfactants on the solubilization of hexachlorobutadiene and hexachloroethane. J Chem Eng Data 62:3252–3260. doi: 10.1021/acs.jced.7b00320

Sabot R, Jeannin M, Gadouleau M, Guo Q, Sicre E, Refait P (2007) Influence of lactate ions on the formation of rust. Corros Sci 49:1610–1624. doi: 10.1016/j.corsci.2006.10.004

Sarathy V, Tratnyek PG, Nurmi JT, Baer DR, Amonette JE, Chun CL, Penn RL, Reardon EJ (2008) Aging of iron nanoparticles in aqueous solution: Effects on structure and reactivity. J Phys Chem C 112:2286–2293. doi: 10.1021/jp0777418

Schöftner P, Waldner G, Lottermoser W, Stöger-Pollach M, Freitag P, Reichenauer TG (2015) Electron efficiency of nZVI does not change with variation of environmental parameters. Sci Total Environ 535:69–78. doi: 10.1016/j.scitotenv.2015.05.033

Shi Z, Fan D, Johnson RL, Tratnyek PG, Nurmi JT, Wu Y, Williams KH (2015) Methods for characterizing the fate and effects of nano zerovalent iron during groundwater remediation. J Contam Hydrol 181:17–35. doi: 10.1016/j.jconhyd.2015.03.004

Shi Z, Nurmi JT, Tratnyek PG (2011) Effects of nano Zero-valent iron on oxidation−reduction potential. Environ Sci Technol 45:1586–1592. doi: 10.1021/es103185t

Shih Y, Chen M-Y, Su Y-F (2011) Pentachlorophenol reduction by Pd/Fe bimetallic nanoparticles: Effects of copper, nickel, and ferric cations. Appl Catal B Environ 105:24–29. doi: 10.1016/j.apcatb.2011.03.024

Song H, Carraway ER (2005) Reduction of chlorinated ethanes by nanosized zero-valent iron: Kinetics, pathways, and effects of reaction conditions. Environ Sci Technol 39:6237–6245. doi: 10.1021/es048262e

Sriwatanapongse W, Reinhard M, Klug CA (2006) Reductive hydrodechlorination of trichloroethylene by palladium-on-alumina catalyst: 13C solid-state NMR study of surface reaction precursors. Langmuir 22:4158–4164. doi: 10.1021/la053087g

Stefaniuk M, Oleszczuk P, Ok YS (2016) Review on nano zerovalent iron (nZVI): From synthesis to environmental applications. Chem Eng J 287:618–632. doi: 10.1016/j.cej.2015.11.046

Stringer R, Johnston P (2001) Chlorine and the Environment: An Overview of the Chlorine Industry. Kluwer Academic Publishers

Sun Y-P, Li X, Cao J, Zhang W, Wang HP (2006) Characterization of zero-valent iron nanoparticles. Adv Colloid Interface Sci 120:47–56. doi: 10.1016/j.cis.2006.03.001

Sun Y, Li J, Huang T, Guan X (2016) The influences of iron characteristics, operating conditions and solution chemistry on contaminants removal by zero-valent iron: A review. Water Res 100:277–295. doi: 10.1016/j.watres.2016.05.031

Tang F, Xin J, Zheng X, Zheng T, Yuan X, Kolditz O (2017a) Effect of solution pH on aging dynamics and Surface structural evolution of mZVI particles: H2 production and spectroscopic/microscopic evidence. Environ Sci Pollut Res 1–11. doi: 10.1007/s11356-017-9976-3

Tang S, Wang X, Liu S, Yang H, Xie YF, Yang X (2017b) Mechanism and kinetics of halogenated compound removal by metallic iron: Transport in solution, diffusion and reduction within corrosion films. Chemosphere 178:119–128. doi: 10.1016/j.chemosphere.2017.03.006

Tosco T, Papini MP, Cruz Viggi C, Sethi R (2014) Nanoscale zerovalent iron particles for groundwater remediation: A review. J Clean Prod 77:10–21. doi: 10.1016/j.jclepro.2013.12.026

Velimirovic M, Auffan M, Carniato L, Batka VM, Schmid D, Wagner S, Borschneck D, Proux O, von der Kammer F, Hofmann T (2018) Effect of field site hydrogeochemical conditions on the corrosion of milled

zerovalent iron particles and their dechlorination efficiency. Sci Total Environ 618:1619–1627. doi: 10.1016/j.scitotenv.2017.10.002

Velimirovic M, Carniato L, Simons Q, Schoups G, Seuntjens P, Bastiaens L (2014) Corrosion rate estimations of microscale zerovalent ironparticles via direct hydrogen production measurements. J Hazard Mater 270:18–26. doi: 10.1016/j.jhazmat.2014.01.034

Velimirovic M, Chen H, Simons Q, Bastiaens L (2012) Reactivity recovery of guar gum coupled mZVI by means of enzymatic breakdown and rinsing. J Contam Hydrol 142–143:1–10. doi: 10.1016/j.jconhyd.2012.09.003

Velimirovic M, Larsson P-O, Simons Q, Bastiaens L (2013a) Reactivity screening of microscale zerovalent irons and iron sulfides towards different CAHs under standardized experimental conditions. J Hazard Mater 252–253:204–212. doi: 10.1016/j.jhazmat.2013.02.047

Velimirovic M, Larsson P-O, Simons Q, Bastiaens L (2013b) Impact of carbon, oxygen and sulfur content of microscale zerovalent iron particles on its reactivity towards chlorinated aliphatic hydrocarbons. Chemosphere 93:2040–2045. doi: 10.1016/j.chemosphere.2013.07.034

Velimirovic M, Simons Q, Bastiaens L (2015) Use of CAH-degrading bacteria as test-organisms for evaluating the impact of fine zerovalent iron particles on the anaerobic subsurface environment. Chemosphere 134:338–345. doi: 10.1016/j.chemosphere.2015.04.068

Voogt EH, Mens AJM, Gijzeman OLJ, Geus JW (1996) XPS analysis of palladium oxide layers and particles. Surf Sci 350:21–31. doi: 10.1016/0039-6028(96)01028-X

Wang J, Chu L (2016) Biological nitrate removal from water and wastewater by solid-phase denitrification process. Biotechnol Adv 34:1103–1112. doi: 10.1016/j.biotechadv.2016.07.001

Wang X, Chen C, Chang Y, Liu H (2009) Dechlorination of chlorinated methanes by Pd/Fe bimetallic nanoparticles. J Hazard Mater 161:815–823. doi: 10.1016/j.jhazmat.2008.04.027

Wei Y-T, Wu S-C, Chou C-M, Che C-H, Tsai S-M, Lien H-L (2010) Influence of nanoscale zero-valent iron on geochemical properties of groundwater and vinyl chloride degradation: A field case study. Water Res 44:131–140. doi: 10.1016/j.watres.2009.09.012

760 Wei Y-T, Wu S, Yang S-W, Che C-H, Lien H-L, Huang D-H (2012) Biodegradable surfactant stabilized
761 nanoscale zero-valent iron for in situ treatment of vinyl chloride and 1,2-dichloroethane. J Hazard Mater
762 211–212:373–380. doi: 10.1016/j.jhazmat.2011.11.018

763 Wu DL, Liu YX, Liu ZG, Ma LM (2014) Dechlorination of hexachloroethane in water using iron shavings and
764 amended iron shavings: Kinetics and pathways. J Chem 2014:1–9. doi: 10.1155/2014/325879

765 Xie Y, Cwiertny DM (2013) Chlorinated solvent transformation by palladized zerovalent iron: Mechanistic
766 insights from reductant loading studies and solvent kinetic isotope effects. Environ Sci Technol 47:7940–
767 7948. doi: 10.1021/es401481a

768 Xu Y, Wang C, Hou J, Wang P, You G, Miao L, Lv B, Yang Y, Zhang F (2017) Application of zero valent iron
769 coupling with biological process for wastewater treatment: A review. Rev Environ Sci Bio/Technology 1–
770 27. doi: 10.1007/s11157-017-9445-y

771 Yan W, Herzing AA, Li X, Kiely CJ, Zhang W (2010) Structural evolution of Pd-doped nanoscale zero-valent
772 iron (nZVI) in aqueous media and implications for particle aging and reactivity. Environ Sci Technol
773 44:4288–4294. doi: 10.1021/es100051q

774 Yan W, Lien H-L, Koel BE, Zhang W (2013) Iron nanoparticles for environmental clean-up: Recent
775 developments and future putlook. Environ Sci Process Impacts 15:63–77. doi: 10.1039/C2EM30691C

776 Yang Y, Cápiro NL, Marcet TF, Yan J, Pennell KD, Löffler FE (2017a) Organohalide respiration with
777 chlorinated ethenes under low pH conditions. Environ Sci Technol 51:8579–8588. doi:
778 10.1021/acs.est.7b01510

779 Yang Y, Cápiro NL, Yan J, Marcet TF, Pennell KD, Löffler FE (2017b) Resilience and recovery of
780 dehalococcoides mccartyi following low pH exposure. FEMS Microbiol Ecol 93:fix130. doi:
781 10.1093/femsec/fix130

782 Yu R-F, Chi F-H, Cheng W-P, Chang J-C (2014) Application of pH, ORP, and DO monitoring to evaluate
783 chromium(VI) removal from wastewater by the nanoscale zero-valent iron (nZVI) process. Chem Eng J
784 255:568–576. doi: 10.1016/j.cej.2014.06.002

785 Zhang W (2003) Nanoscale iron particles for environmental remediation: An overview. J Nanoparticle Res
786 5:323–332. doi: 10.1023/A:1025520116015

787 Zhao X, Liu W, Cai Z, Han B, Qian T, Zhao D (2016) An overview of preparation and applications of stabilized
788 zero-valent iron nanoparticles for soil and groundwater remediation. Water Res 100:245–266. doi:
789 10.1016/j.watres.2016.05.019

790 Zhu B-W, Lim T-T, Feng J (2008) Influences of amphiphiles on dechlorination of a trichlorobenzene by
791 nanoscale Pd/Fe: Adsorption, reaction kinetics, and interfacial interactions. Environ Sci Technol 42:4513–
792 4519. doi: 10.1021/es800227r

793 Zhu C, Zhu F, Liu C, Chen N, Zhou D, Fang G, Gao J (2018) Reductive hexachloroethane degradation by
794 $S_2O_8^{\bullet-}$ with thermal activation of persulfate under anaerobic conditions. Environ Sci Technol 52:8548–
795 8557. doi: 10.1021/acs.est.7b06279

796

List of tables

Table 1 Pseudo-first order rate constants for HCA degradation under the different experimental conditions (effects of Pd-mZVI dosage, temperature, HCA initial concentration and PLA content)

Figure number	$m_{Pd\text{-}mZVI}$ (mg)	T (°C)	$[HCA]_0$ (mg L^{-1})	m_{PLA} (mg)	k_{obs} (Eq. 12) (min^{-1})
4	150	25	10	850	0.002 (R^2 = 0.474)
	375	25	10	850	0.004 (R^2 = 0.860)
4, 5, 6, 7	600	25	10	850	0.035 (R^2 = 0.975)
5	600	12	10	850	0.004 (R^2 = 0.970)
	600	35	10	850	0.093 (R^2 = 0.939)
6	600	25	5	850	0.036 (R^2 = 0.940)
	600	25	20	850	0.010 (R^2 = 0.972)
7	600	25	10	1 700	0.030 (R^2 = 0.938)
	600	25	10	3 400	0.025 (R^2 = 0.951)

List of figures

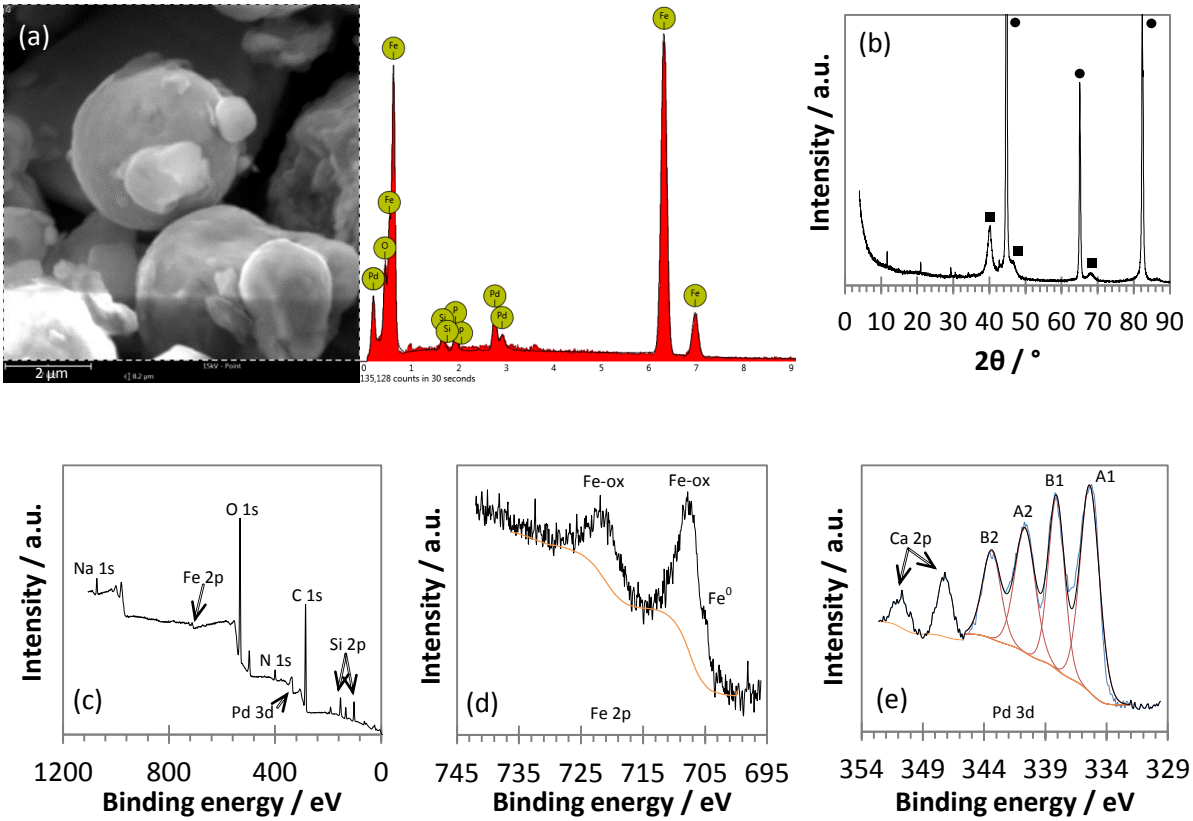

Fig. 1 Characterization of Pd-mZVI particles before reaction. (a) SEM image with EDS spectrum. The atomic concentration in the entire area is: Fe = 77.4%, O = 16.3%, Pd = 3.3%, P = 1.8%, Si = 1.2%; (b) X-ray diffraction pattern, where solid circles and squares represent Fe^0 and Pd^0, respectively; X-ray photoelectron spectra: (c) Survey scan, (d) Fe 2p, (e) Pd 3d

808

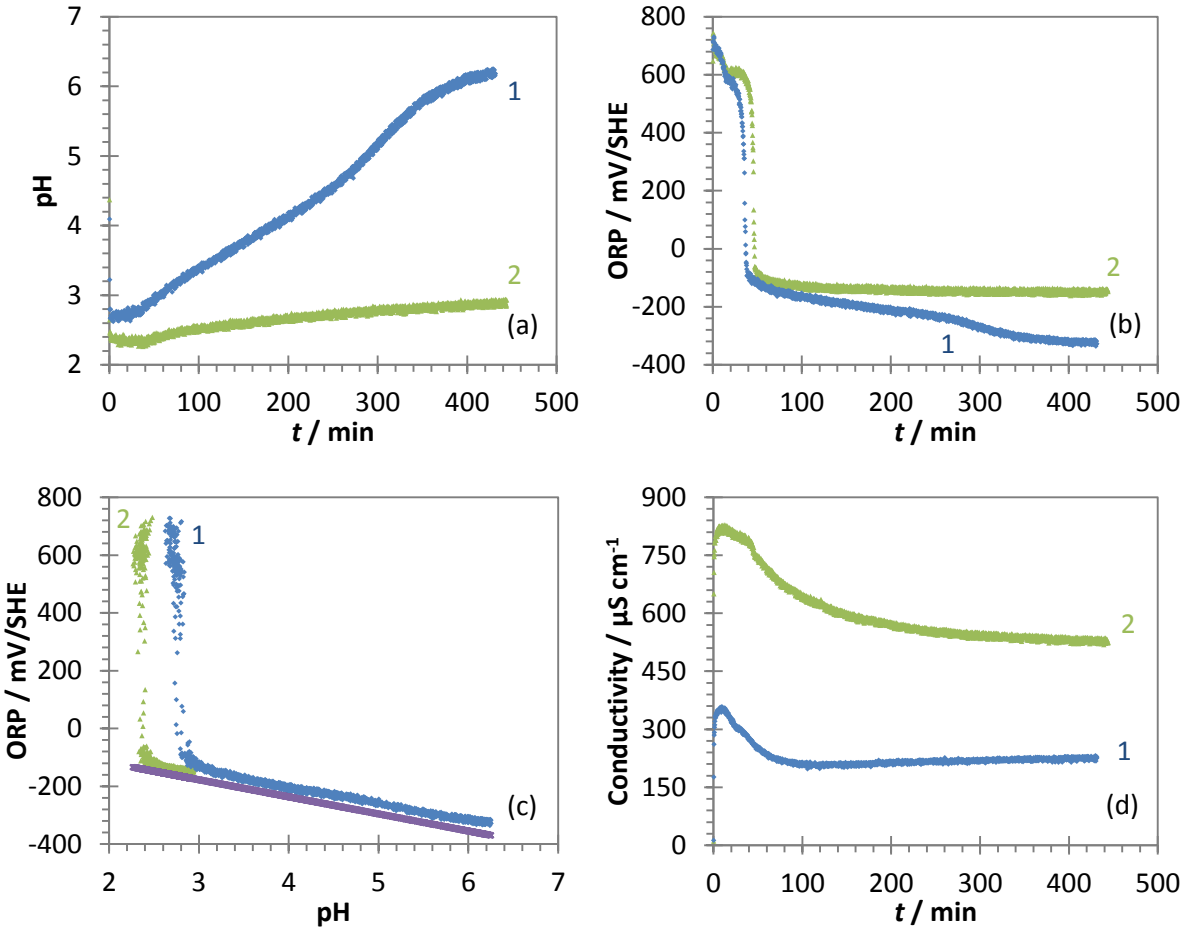

809

810 ◆ (1) = 850 mg PLA, ▲ (2) = 3400 mg PLA, × = H^+/H_2 redox couple

811 **Fig. 2** Monitoring of the aqueous corrosion in the Pd-mZVI/PLA/H_2O system without opening of the reactor.

812 (a) Evolution of pH with time, (b) Evolution of ORP with time, (c) Evolution of ORP with pH, (d) Evolution of

813 conductivity with time. Experimental conditions: $m_{Pd\text{-}mZVI}$ = 600 mg, T = 25 °C

814 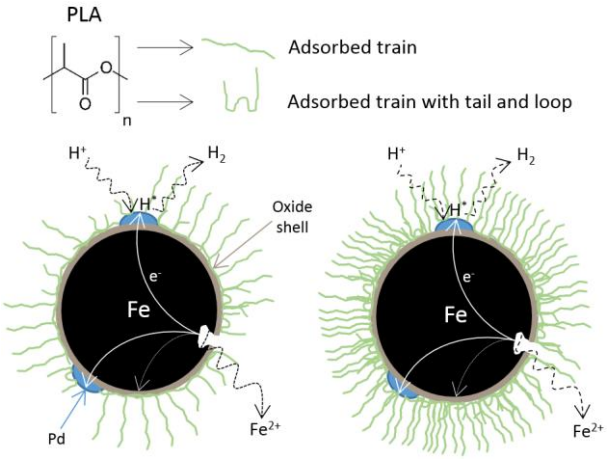

815 **Fig. 3** Schematic illustration of the Pd-mZVI/PLA/H_2O system, with 850 mg (left) and 3400 mg (right) of PLA.
816 Depending on the adsorbed PLA on the surface, it is represented mainly as adsorbed train or as an extended layer
817 of adsorbed train with tails and loops.

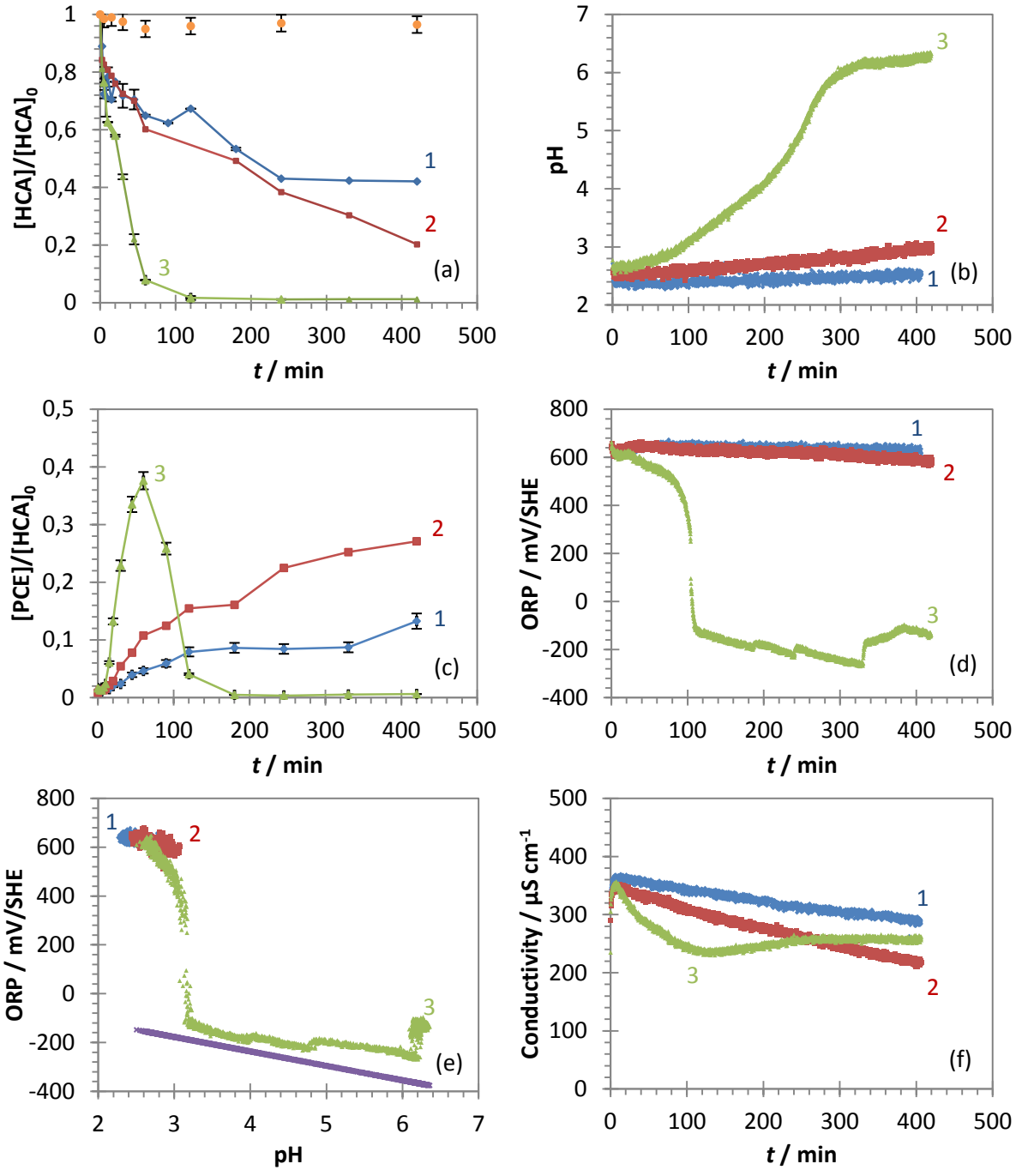

◆ (1) = 150 mg Pd-mZVI, ■ (2) = 375 mg Pd-mZVI, ▲ (3) = 600 mg Pd-mZVI, ● = blank, × = H^+/H_2 redox couple

Fig. 4 Effects of Pd-mZVI dosage on HCA dechlorination in the Pd-mZVI/PLA/HCA/H_2O system. (a) Evolution of HCA concentration with time, (b) Evolution of pH with time, (c) Evolution of PCE concentration with time, (d) Evolution of ORP with time, (e) Evolution of ORP with pH, (f) Evolution of conductivity with time. Experimental conditions: $[HCA]_0$ = 10 mg L^{-1}, m_{PLA} = 850 mg, T = 25 °C. Error bars in parts a and c represent standard deviation for n = 2

827

828

829

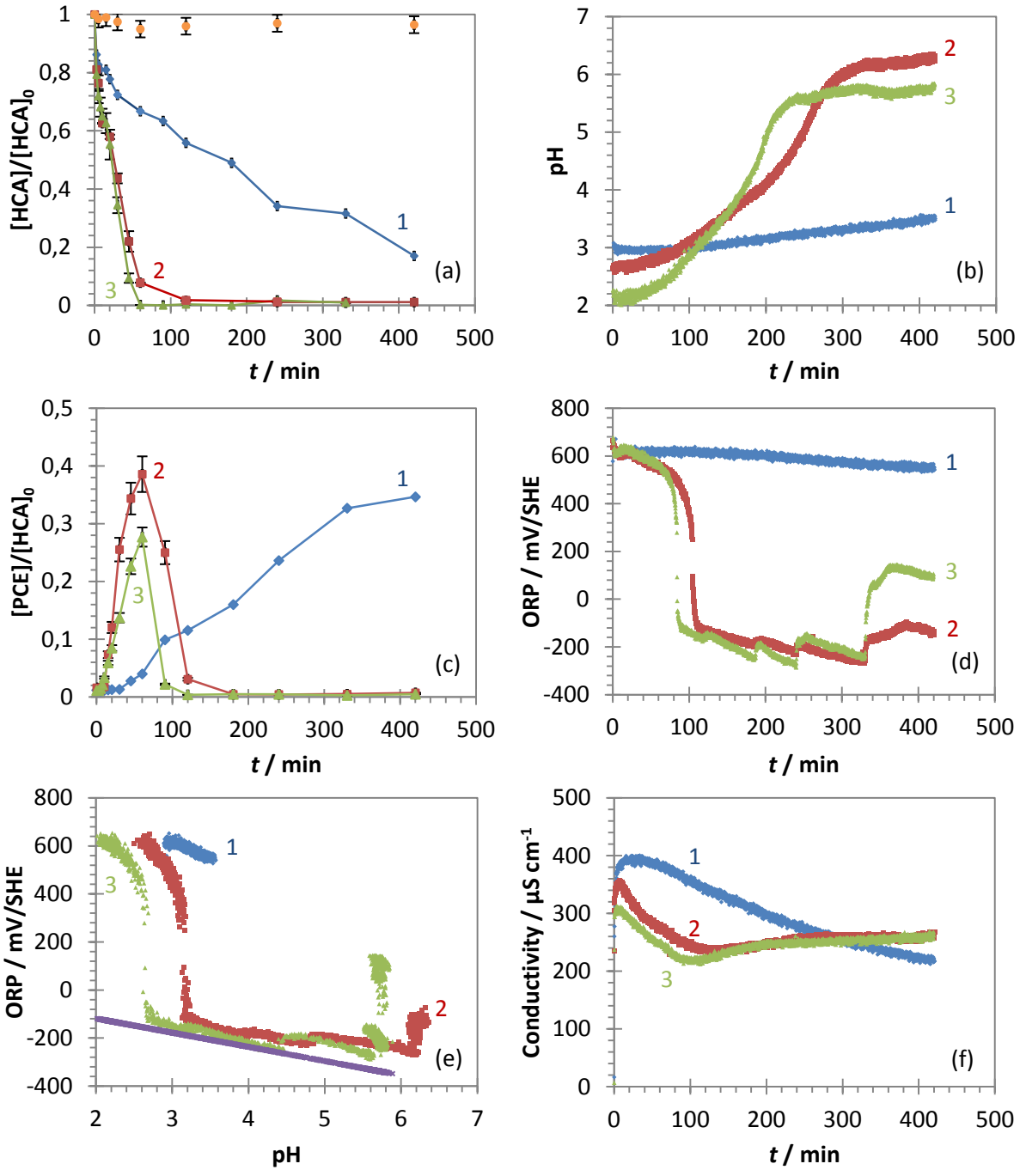

830 ◆ (1) = 12 °C, ■ (2) = 25 °C, ▲ (3) = 35 °C, ● = blank, × = H^+/H_2 redox couple

831 **Fig. 5** Effects of temperature on HCA dechlorination in the Pd-mZVI/PLA/HCA/H_2O system. (a) Evolution of
832 HCA concentration with time, (b) Evolution of pH with time, (c) Evolution of PCE concentration with time, (d)
833 Evolution of ORP with time, (e) Evolution of ORP with pH, (f) Evolution of conductivity with time.
834 Experimental conditions: $[HCA]_0$ = 10 mg L^{-1}, $m_{Pd\text{-}mZVI}$ = 600 mg, m_{PLA} = 850 mg. Error bars in parts a and c
835 represent standard deviation for n = 2

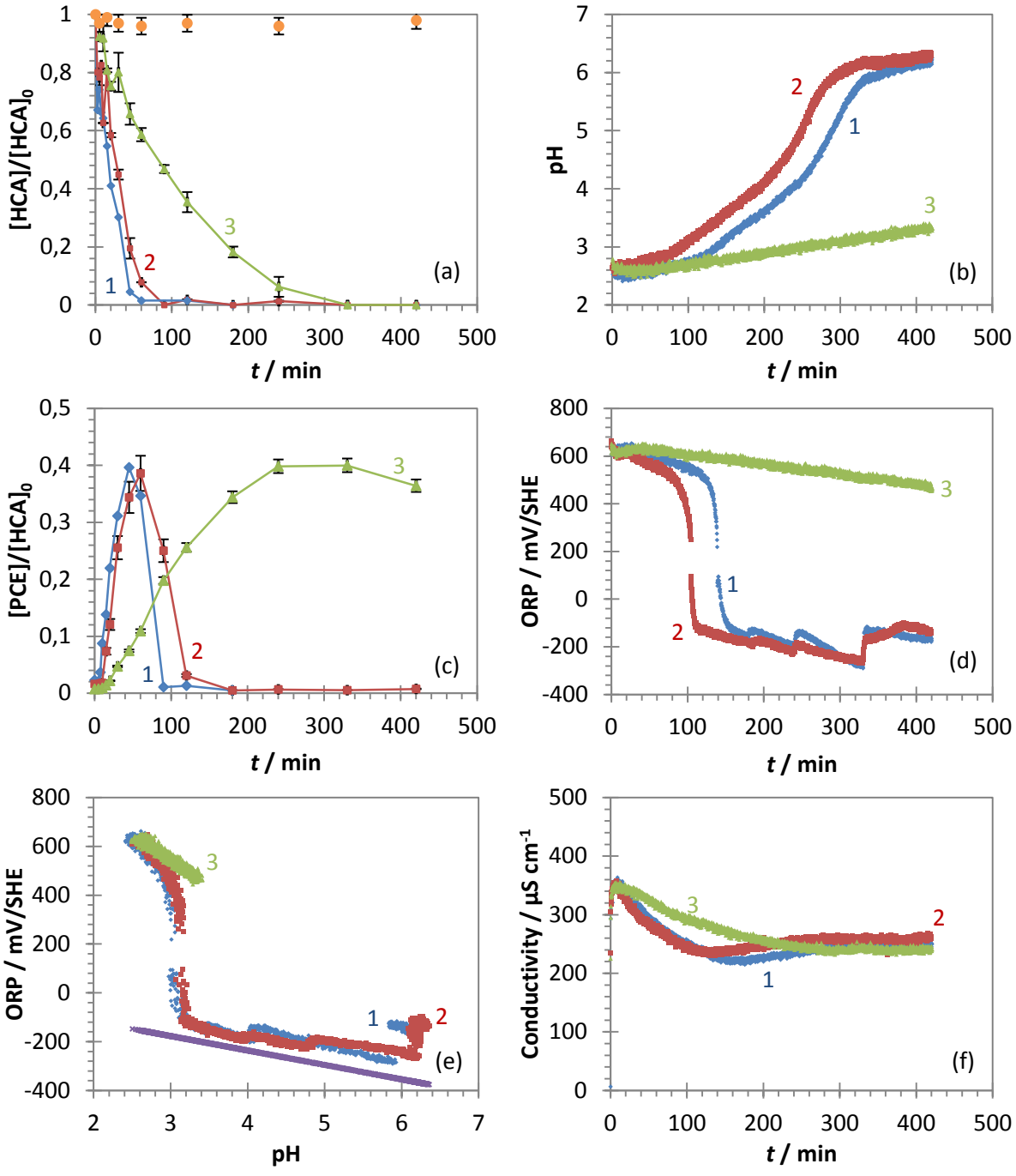

◆ (1) = 5 mg L^{-1}, ■ (2) = 10 mg L^{-1}, ▲ (3) = 20 mg L^{-1}, ● = blank, × = H^+/H_2 redox couple

Fig. 6 Effects of initial HCA concentration on its dechlorination in the Pd-mZVI/PLA/HCA/H_2O system. (a) Evolution of HCA concentration with time, (b) Evolution of pH with time, (c) Evolution of PCE concentration with time, (d) Evolution of ORP with time, (e) Evolution of ORP with pH, (f) Evolution of conductivity with time. Experimental conditions: $m_{Pd\text{-}mZVI}$ = 600 mg, m_{PLA} = 850 mg, T = 25 °C. Error bars in parts a and c represent standard deviation for n = 2

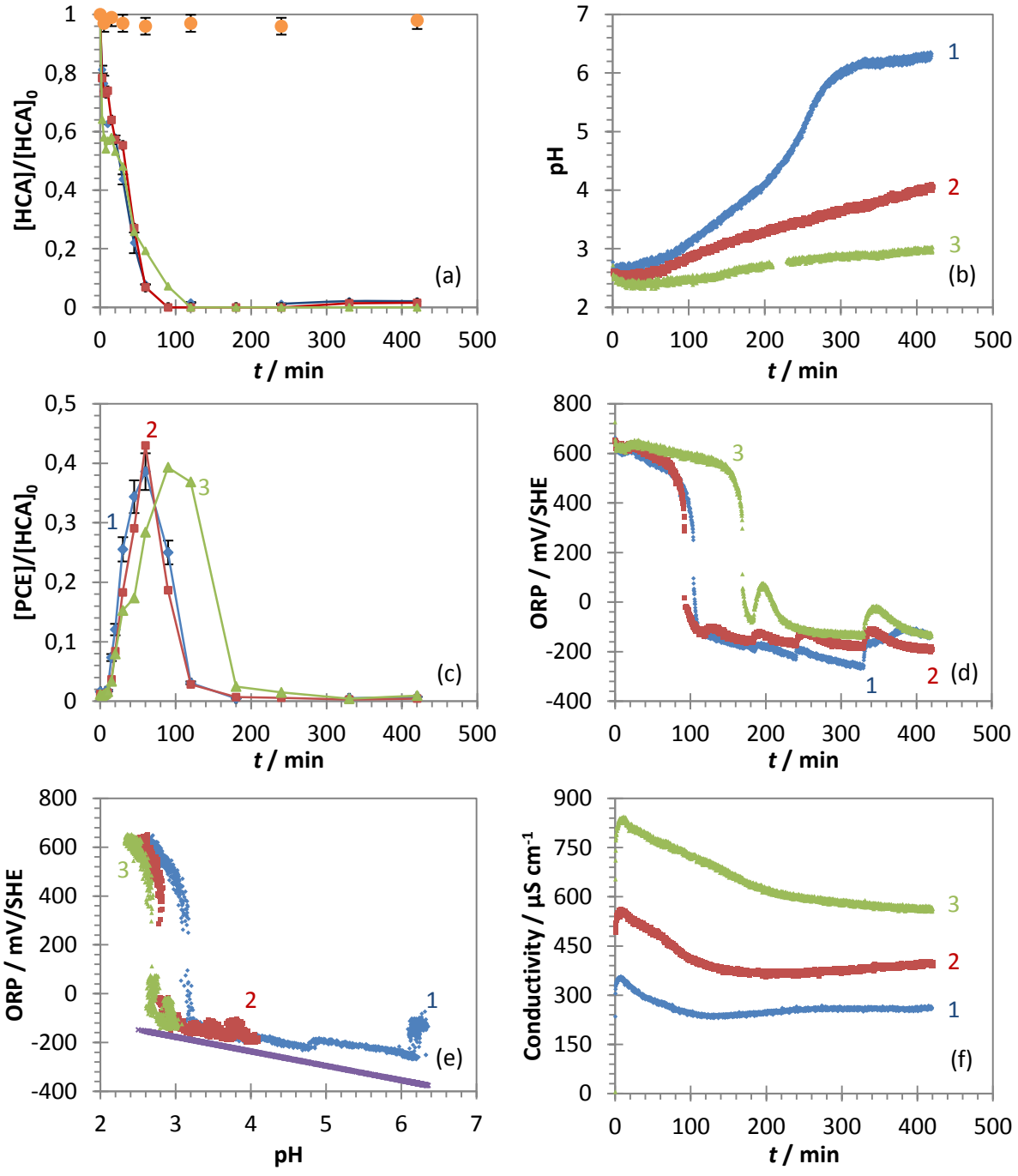

◆ (1) = 850 mg PLA, ■ (2) = 1700 mg PLA, ▲ (3) = 3400 mg PLA, ● = blank, × = H^+/H_2 redox couple

Fig. 7 Influence of PLA content on HCA dechlorination in the Pd-mZVI/PLA/HCA/H_2O system. (a) Evolution of HCA concentration with time, (b) Evolution of pH with time, (c) Evolution of PCE concentration with time, (d) Evolution of ORP with time, (e) Evolution of ORP with pH, (f) Evolution of conductivity with time. Experimental conditions: $[HCA]_0$ = 10 mg L^{-1}, $m_{Pd\text{-}mZVI}$ = 600 mg, T = 25 °C. Error bars in parts a and c represent standard deviation for n = 2

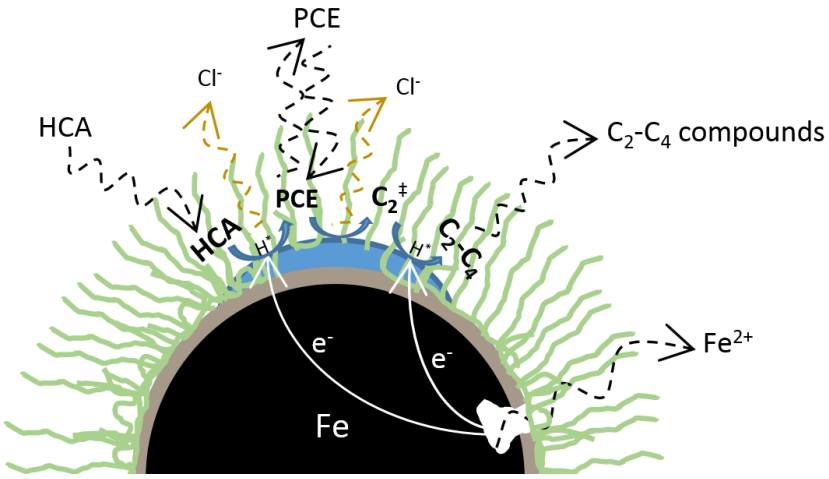

Fig. 8 Schematic illustration of reductive HCA dechlorination in the Pd-mZVI/PLA/HCA/H_2O system. Reactions proposed in Fig. 3 (production of atomic hydrogen H^*) and in this figure (HCA dechlorination) may occur simultaneously